NTNU
Norwegian University of
Science and Technology

Frequency Dependence of Bilge Keels

Simen Haugen Orvedal

Marine Technology
Submission date: June 2018
Supervisor: Håvard Holm, IMT

Norwegian University of Science and Technology
Department of Marine Technology

Preface

This thesis represents the final work of a two year Master's of Science degree in Marine Technology at the Norwegian University of Science and Technology (NTNU), Trondheim. This thesis was written during the spring semester of 2018 and accounts for 30 credits. The thesis is a continuation of a project thesis written in the autumn semester 2017.

I would like to thank my supervisor Associate Professor Håvard Holm at the Department of Marine Technology, NTNU, for his guidance, valuable input and patience throughout the project and masters thesis. I would also like to extend my gratitude to my fellow students Erik Hveding, Simon Drønen, Haakon Nordkvist, Mats Thunes, Sondre Ellingsen and Øystein Bertelsen for discussions and assistance of various sorts.

Trondheim, 2018-06-11

Simen H. Orvedal

Abstract

The goal of this master's thesis is to inspect the damping generated by bilge keels. Two dimensional cross sections have been modeled both with and without bilge keels and simulated using the computational fluid dynamics software STAR-CCM+. The results have been post-processed in order to identify the damping forces using both a linearized approach and a composite model that divides the damping into wave-making and quadratic components. Simulations without bilge keels was compared with results from existing model experiments. Different bilge keel length and tip shapes was simulated and the difference in generated damping is compared.

The motivation for this study is to get a better understanding of the fluid flow around bilge keels in order to achieve better future designs. The due to the accuracy of the simulations, the results are inconclusive. The results indicate that bilge keel has a very limited impact on wave-damping and that the accuracy of damping is highly time-step sensitive and bilge keel length has a large impact on the damping provided.

Sammendrag

Målet med denne masteroppaven er å undersøke dempingskreftene som blir forårsaket av slingrekjøler. Todimensjonale midtskips seksjoner både med og uten slingrekjøler har blitt modellert og simulert ved hjelp av det numeriske fluidynamikk programmet STAR-CCM+. Resultatene har blitt etterbehandlet med det formål av å kalkulere dempingskoeffisientene. To dempingsmodeller har blitt anvendt, en linearisert og en kompositttmodel som deler opp dempingsbidraget i bølge-generert demping og andre ordens demping. Forskjellige slingrekjøllengder og tup geometri har blitt simulert og sammenlignet. Motivasjonen som ligger til grunne for denne oppgaven er å få en bedre forståelse av strømmen av fluid rundt slingrekjøler, for å kunne gjøre forbedringer på fremtidige design. Grunnet for lite nøyaktighet i simuleringene, er konklusjonen mangelful. Resultane indikerer at slingrekjøler har meget begrenset innvirkning på bølgedannelse, simulerings nøyaktighet er særdeles sensitiv til tidsteg og at slingrekjølens lengde har stor innvirkning på mengden demping skapt.

Nomenclature

B Beam length

T Draft

H Height

R Corner Radius

CFD Computational Fluid Dynamics

$\forall$ Submerged volume for a unit length

ρ Water density

ν Dynamic fluid viscosity

g Gravitational Acceleration

ϕ Velocity potential function

ζ Surface elevation of a potential wave

ζ_a Wave amplitude

ω Circular frequency in radians per second

t Time

k Wave number

x, y, z Cartesian Coordinates

u, v, w Velocity Components

p Pressure

p_D Dynamic Pressure

RANS Reynolds-averaged Navier-Stokes

$k-\epsilon$ A turbulence model, see chapter 2.2.2

$k-\omega$ A turbulence model, see chapter 2.2.2

STAR-CCM+ A CFD software

FLUENT A CFD software

$\nabla \cdot \mathbf{F}$ Divergence of F

Overset Mesh A type of mesh used in simulation of motion, see chapter 2.6.1

Prism mesh/layer An approach for near-wall (boundary layer) meshing, see chapter 2.6.2

Base size A cell size which all mesh cell sizes are derived from, see chapter 2.6

DOF / η A degree of freedom

$\dot{\eta}$ The velocity of a DOF

$\ddot{\eta}$ The acceleration of a DOF

η_a Amplitude of a degree of freedom, used for imposed motion, see chapter **??**

a_{44} Added roll inertia coefficient

a_{24} Coupled added mass in sway-roll coefficient

a^*_{44} Non-dimensional added roll inertia coefficient

a^*_{24} Non-dimensional coupled added mass in sway-roll coefficient

b_{44} Roll damping coefficient (linear)

b_{24} Sway-Roll damping coefficient

b^*_{44} Non-dimensional roll damping coefficient

b^*_{24} Non-dimensional coupled sway-roll damping coefficient

$b^{'}_{44}$ Quadratic damping coefficient

b^w_{44} Linear wave-damping coefficient

c_{44} Roll stiffness coefficient / Hydrostatic moment coefficient

ω^* Dimensionless circular frequency

GZ Right arm, the horizontal distance between center of buoyancy and center of rotation

$M_4(t)$ Roll moment time series

$\hat{M}_4(t)$ Hydrodynamic roll moment time series, see chapter 2.7.2

$\dot{W}$ Time averaged mechanical power

$\dot{E}$ Energy flux of radiating waves

$|A_+|$ Upstream wave amplitude

$|A_-|$ Downstream wave amplitude

Contents

List of Figures

List of Tables

Chapter 1

Introduction

Roll motion of ships has historically been a challenging degree of freedom to predict. Unlike translational movements, such as heave, the motion damping is not dominated by wave generation and viscous damping is of significant importance. Several systems has been invented in order reduce the roll movement by adding damping, a few examples of which is anti-roll tanks, roll stabilization fins and bilge keels. The former is the focus of this thesis.

Bilge keels, in its simplest form, are plates mounted normal to the hull of a vessel that is intended to induce flow separation from roll motion. Often they are placed along the midship section of a vessel with varying depth from 1-3% of the ship beam (Pettersen, 2007).

Bilge keels has been used since the age of William Froude, whom advocated the use of "bilge pieces" to be placed normal to the ship bottom at the corner of the bilge (Froude, 1865). Since then several empirical methods have been developed to predict the effect of bilge keels (Kato (1965), Ikeda et al. (1977b)).

In more recent years predictions methods based on solving the flow has been utilized. Yeung et al. developed and employed a free-surface random vortex method code to solve the flow of a rolling two-dimensional cross section and accurately predict the hydrodynamic coefficients for hulls with and without bilge keels with remarkable accuracy (Yeung and Vaidhyanathan (1994), Yeung et al. (1998), Yeung et al. (2001)). Quérard et al. showed that a Reynolds-Averaged Navier-Stokes approach is able to replicate experimental values in roll, sway and heave for cross sections without bilge keels.

A consistent benchmark used by both Yeung and Quérard is the experimental results found by Ir J.H. Vugts, whom calculated cross sectional hydrodynamic coefficients from the resulting moment on rectangular cylinders from an imposed harmonic rolling motion on the free surface (Vugts, 1968). This experimental data will be used as experimental comparison for this thesis and can be found in appendix B.

An important application of two-dimensional coefficients is strip theory. By dividing the submerged part of, for instance, a ship into strips (cross sections), then calculating the added mass and damping for each strip and integrating the coefficients along the length of the ship an approximation of the total hydrodynamic properties of the vessel is found (Faltinsen, 1993).

1.1 Scope of Work

The main objective of this thesis is to inspect the damping induced by bilge keels. In order to achieve this goal, the work is divided into four parts:

1. Model cross sections with and without bilge keels
2. Inspect the impact of bilge keel length and tip geometry on damping by simulating harmonic motion
3. Compare the calculations with available experimental results
4. Simulate the roll response of incoming waves

1.2 Limitations

The study is limited to two dimensional systems and single degree-of-freedom motion in roll.

Chapter 2

Methods

2.1 Damping

Damping in its simplest form can be described as system forces that is due to the velocity of a motion. For a rolling vessel the damping is due to wave-making and viscous effects. Viscous damping can be divided into skin friction and eddy-making damping, for full scale vessels the skin friction is negligible, eddy-making damping is non-linear and expressed on the form $b_{44}\dot{\eta}_4|\dot{\eta}_4|$ (Faltinsen, 1993).

Whether the eddy-making or wave-making damping is dominating the roll motion is dependent upon the vessel geometry, frequency of oscillations and amplitude of the motion (Ikeda et al., 1977a). This can be illustrated by considering a one degrees of freedom system, where first- and second-order damping occurs with coefficients of equal unit value:

$$-m\ddot{\eta} - b^{1st}\dot{\eta} - b^{2nd}\dot{\eta}|\dot{\eta}| - c\eta = F(t) \tag{2.1}$$

Due to the quadratic nature of the second order term, it will dominate the total damping contributions at high velocities. This is illustrated in figure 2.1.

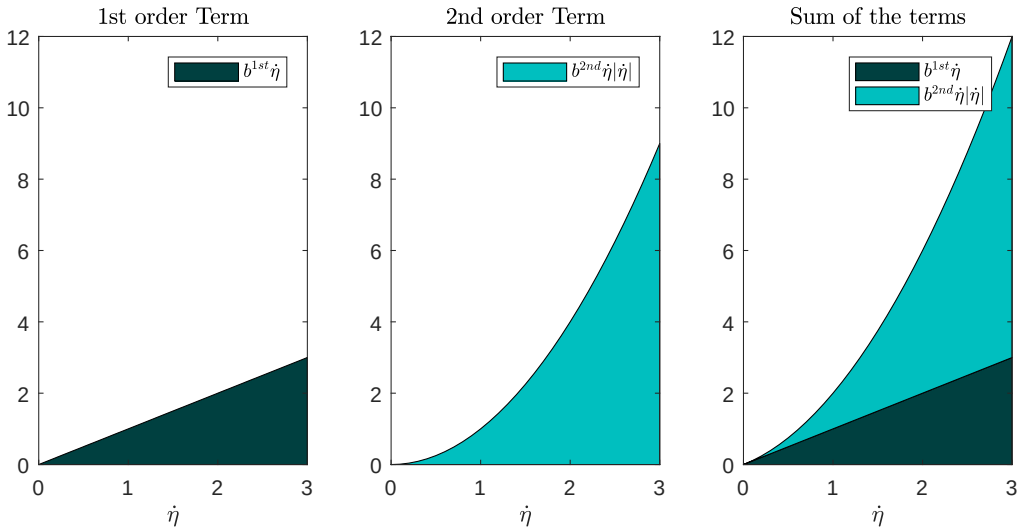

Figure 2.1: A sketch showing how quadratic damping forces dominates at high velocities.

2.2 Numerical Approach

STAR-CCM+ is an all purpose computational fluid dynamics software, and as such has the ability to simulate a wide range of physical phenomenons by combining different physical models. In the following subsections brief explanations of the most important models is presented. In appendix A a complete list of physical models used is presented.

2.2.1 Reynolds-Averaged Navier-Stokes

The numerical flow solver in STAR-CCM+ uses a finite volume discretization approach to transform the Reynolds-Averaged Navier-Stokes (RANS) equations into a system of algebraic equations [SIEMENS (2017)]. The RANS equations used in the solver can be thought of as time-averaging for steady-state situations or ensemble averaging for transient situations. The general form of the RANS equations used in the solver are

$$\frac{\partial \rho}{\partial t} + \nabla \cdot [\rho(\bar{\mathbf{v}} - \mathbf{v}_g)] = 0 \tag{2.2}$$

$$\frac{\partial}{\partial t}(\rho\bar{\mathbf{v}}) + \nabla \cdot [\rho(\bar{\mathbf{v}} - \mathbf{v}_g)] = -\nabla \cdot \bar{p}\mathbf{I} + \nabla \cdot (\mathbf{T} + \mathbf{T_t}) + \mathbf{f_b} \tag{2.3}$$

where ρ is the fluid density, $\bar{\mathbf{v}}$ mean velocity vector, $\bar{p}$ mean pressure, $\mathbf{v}_g$ reference frame velocity relative to the laboratory frame, $\mathbf{I}$ identity tensor, $\mathbf{T}$ viscous tensor, $\mathbf{T_t}$ Reynolds stress tensor and $\mathbf{f_b}$ is the body forces (gravity).

2.2.2 K-ϵ Turbulence Model

To close the governing equations it is necessary to use a turbulence model to calculate the Reynolds stress tensor. The k-ϵ model is applied, which solves two transport equations for turbulent kinetic energy k and turbulent dissipation rate ϵ [Jones and Launder (1972)].

STAR-CCM+ supports three main variations of k-ϵ turbulence modeling; High-Reynolds number approach, Low-Reynolds number approach and the two layer approach. In this thesis the two layer approach, first proposed by Rodi (Rodi, 1991), is used. The two layer approach, divides the computation into a near wall layer and the remaining domain. The latter is solved with the original k-ϵ model. Flow near the walls is solved by utilizing a turbulent dissipation rate (ϵ) and turbulent viscosity specified as functions of wall distance with a smoothed transition to the dissipation rate and viscosity far from the wall.

The k-ϵ model has been applied in example case studies by the STAR-CCM+ user guide for similar free-surface simulation types, in addition to being a good compromise between computational cost, accuracy and robustness (SIEMENS, 2017). Other works, however, has shown that several turbulence models can be applied and accurately capture the roll motion, such as the k-ϵ SST model first proposed by Menter (1994) and applied by Quérard et al. (2009). Ultimately, the k-ϵ model was chosen due to the limitation of computational power and the recommendation of the software user guide.

2.2.3 Volume of Fluid

To account for the free surface it is necessary to apply an additional transport equation which introduces a scalar representing the volume of fluid (VOF)(SIEMENS, 2017). The scalar is a specific cells fraction fluids, meaning that a cell with VOF-scalar of 1 is filled with water while a cell with 0 contains no water and only air. The surface elevation is defined as the point at which the scalar is equal to 0.5 and is found by interpolation. A cells fluid viscosity and density is the average value between the two fluids weighted by the volume fraction scalar.

The fluids are defined as phases using a Eulerian multiphase model. Both air and water is defined as incompressible fluids with default density and viscosity values, as presented in table 2.1.

Table 2.1: Fluid Properties

Fluid	Density (ρ)	Dynamic Viscosity (μ)
Water	$997.561\left[\frac{kg}{m^3}\right]$	$8.88710E-4\left[\frac{Pa}{s}\right]$
Air	$1.18415\left[\frac{kg}{m^3}\right]$	$1.85508E-5\left[\frac{Pa}{s}\right]$

2.2.4 Implicit Unsteady

Time was modeled using the an implicit unsteady solver which uses a constant user defined time-step and inner iterations within each step. The inner iterations converge the solution for the given instant in time, by use of a spatial integration scheme (SIEMENS, 2017). Implicit unsteady is chosen by the same reasoning as the k-ϵ turbulence model; the solver is applied in similar example case studies by the STAR-CCM+ user guide. In addition the implicit unsteady model is recommend for simulations where vortex shedding is of importance and/or the time-varying boundary conditions. This is particularly fitting for wave-response simulations (see subsection 2.4.6)

2.3 Geometry of the Cross section

Two different cross sections geometries, with and without bilge keels fitted, are used in this thesis. Both have a base shape of a square rectangle with rounded bottom corners, beam length of 400 millimeters and a draft equal to half the beam length. The only distinguishing feature between the two is the magnitude of the corner radius. A small corner radius of 2.5 millimeters is used in order to compare the results with available experimental data. This corresponds to the exact same geometry simulated by Vugts (1968). However, very few vessel have midsection with such sharp corner radii. Therefore a cross section with a 50 millimeter corner radius is also used when comparing the impact of bilge keel length and tip geometry. In figure 2.2 the two cross sections are shown, without bilge keels.

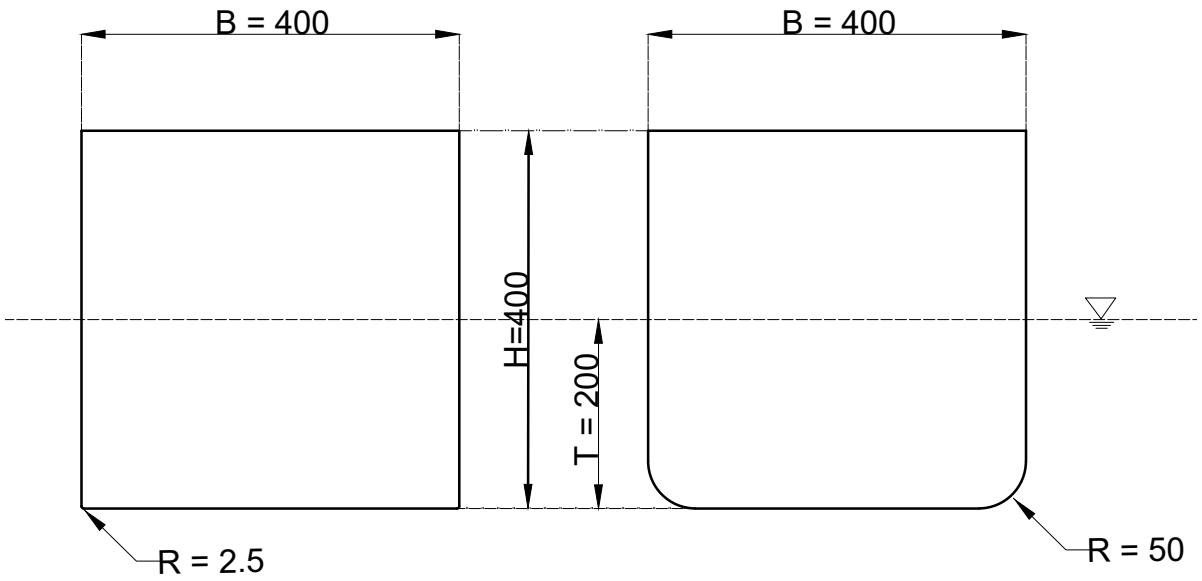

Figure 2.2: The base cross-sectional geometry with dimensions in millimeters

2.3.1 Bilge Keel Geometry

The bilge keels are fitted to the base geometry at a 45 degree angle (relative to the waterline) on the center of the corner arcs. The bilge keels all have equal thickness. In figure 2.3 the three different bilge keel lengths are shown.

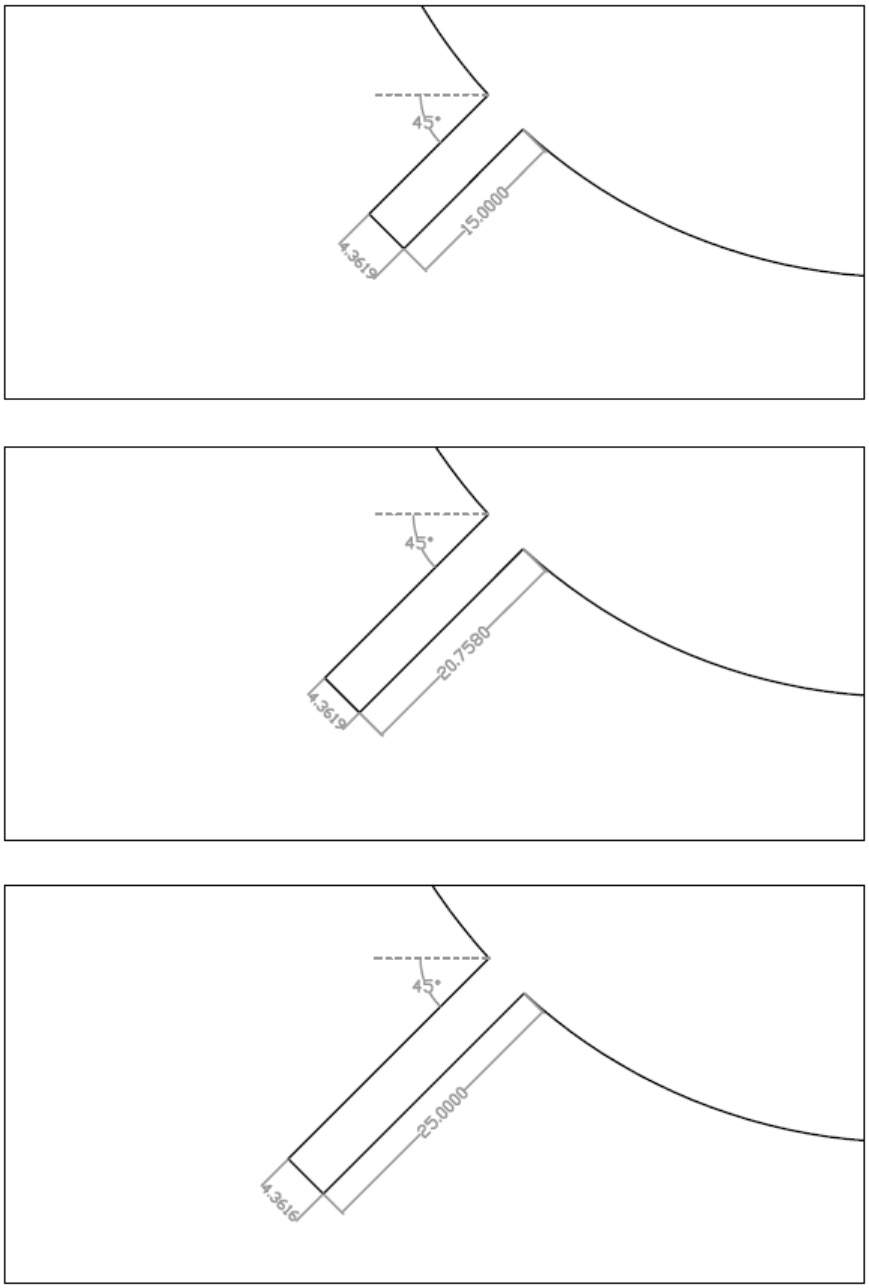

Figure 2.3: Close up illustration of the bilge keel geometry with dimensions in millimeters and degrees

The bilge keels themselves are, as seen in figure 2.3, shaped as simple rectangles. The different lengths are chosen such that they are steadily increasing by 5 mm, with the exception of the middle length which is slightly increased to be the exact same length as the alternative tip design.

The alternative tip shape is modelled as a right isosceles triangle, as seen in figure 2.4.

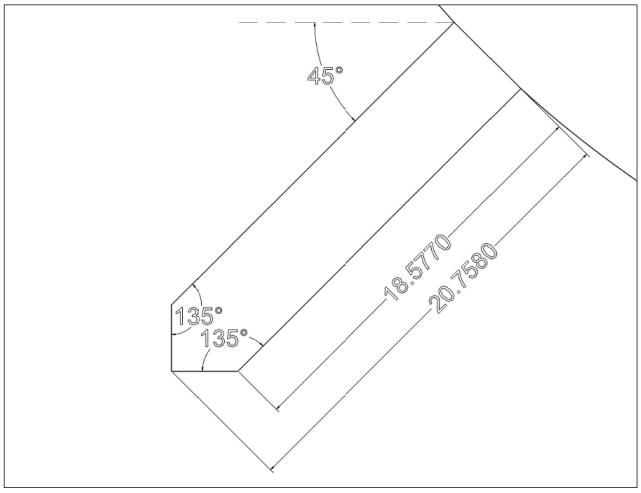

Figure 2.4: The alternative bilge keel tip shape, shown with dimension in millimeters

For wave-response tests, the bilge keels are fitted to the corner at a 45 degree angle. This can be seen in figure 2.5. The width is chosen such that the bilge keel intersects the hull at would have otherwise been the start of the corner rounding.

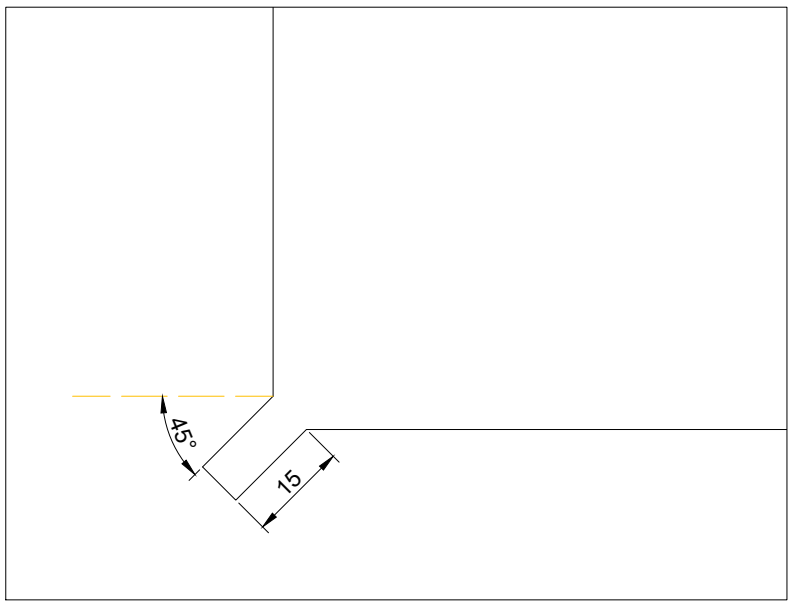

Figure 2.5: Bilge keel geometry for wave-response tests with dimensions in millimeters and degrees

2.4 Boundary Conditions

In order to solve the RANS equations described in chapter 2.2.1, the boundaries of the fluid domain needs to be defined. The boundary conditions applied in this thesis are:

- Velocity Inlet
- Pressure Outlet
- Wall
- Symmetry Plane
- Overset Border

In the following subsections a brief general explanation of what the different boundary conditions are and how they are applied in this thesis is presented.

2.4.1 Velocity Inlet

A velocity inlet is a boundary condition that describes a known inflow. A defined fluid velocity and angle at the boundary is enforced on the mesh cells next to the boundary. In the case of multiphase flows the distribution of fluids must also be defined.

For free surface simulations it's necessary to define a calm water free surface under which the fluid inflow is pure water, and above which the inflow is pure water. This is done through a user field function, which creates binary volume fraction value for the entire domain. An example user field function syntax for a calm water simulation is:

```
($$ Position[1]<=0)?0:1
```

Where $$Position[1] is the y-coordinate of a cell and <= is a boolean less or equal operator. In other words, the syntax is an if statement evaluating whether or not the current y-coordinate is above the calm water free surface (set to y=0) and assigning a water volume fraction value of 0 to positions above the free surface and a value of 1 for positions below. The inflow velocity of free surface simulations is set to be zero meters per second.

2.4.2 Pressure Outlet

A pressure outlet defines a constant pressure gradient across the boundary condition. The condition is enforced by defining the velocity through the boundary such that the pressure gradient is constant across the border. Both the pressure gradient and the fluid distribution must be defined. The fluid distribution is defined by the same user field function as the velocity inlet

(2.4.1). A pressure gradient derived from hydrostatic pressure and implemented by use of user field functions is used for calm water simulations. An example syntax for such a field function is:

```
($$ Position[1]<=0)?0:(-${ DensityWater }*9.81*$$ Position[1])
```

Similar to the volume fraction function the pressure gradient field function starts of with an if statement evaluating whether or not the current position is above the free surface. However, unlike the volume fraction function the pressure gradient field function assigns a calculated hydrostatic pressure values instead of volume fraction.

2.4.3 Wall

The wall boundary condition models a impenetrable surface. For this thesis all walls has no-slip conditions, meaning that the fluid on the surface sticks to the surface. For a moving hull this means that the fluid on the wall has a velocity equal to the hull.

2.4.4 Symmetry Plane

A symmetry plane has zero fluid shear stress and the velocity and pressure is computed by extrapolating the values from the adjacent cell using reconstruction gradients. This boundary condition represents a plane that has symmetric flow to the adjacent plane within the domain.

2.4.5 Overset Border

The overset boundary conditions is the boundary condition that allows for use of overset interfaces between domain meshes and overset regions, as described in subsection 2.6.1. The surface of the boundary condition must be within a larger existing fluid domain.

2.4.6 Boundary Conditions for Linear Wave Simulations

The wave motion simulations attempts to simulate linear potential theory waves, according to a velocity potential function (Faltinsen, 1993) for a wave in infinite water depth on the form:

$$\phi = \frac{g\zeta_a}{\omega} e^{kz} \cos(\omega t - kx) \tag{2.4}$$

where ζ_a is the wave amplitude and k is the wave number. The velocity potential function 2.4 corresponds to a wave profile on the form:

$$\zeta = \zeta_a \sin(\omega t - kx) \tag{2.5}$$

The x and z velocity components and dynamic pressure function is found by derivation of the potential function:

$$u = \frac{d\phi}{dx} = \omega\zeta_a e^{kz}\sin(\omega t - kx) \tag{2.6}$$

$$w = \frac{d\phi}{dz} = \omega\zeta_a e^{kz}\cos(\omega t - kx) \tag{2.7}$$

$$p_D = -\rho\frac{d\phi}{dt} = \rho g\zeta_a e^{kz}\sin(\omega t - kx) \tag{2.8}$$

The velocity inlet uses a user field function defined according to the velocity components in equation 2.6 and 2.7 in order to account for the changing velocity of a linear wave. The free surface is defined similarly as described in section 2.4.1. However, instead of using a calm water line, the if statement checks whether or not a points is under or above the wave profile defined in equation 2.5. The free surface user field function is used to account for volume fraction of fluid for both velocity inlets and pressure outlets.

The pressure outlet needs to account for both the hydrostatic pressure and the hydrodynamic pressure of the linear wave. Therefore, the user field function for the pressure field is defined as the sum of hydrostatic pressure (as described in subsection 2.4.2) and the hydrodynamic pressure given by equation 2.8.

2.5 Simulation Setup

2.5.1 Fully Submerged Simulations

The simplest simulation setup that is conducted in this thesis is a fully submerged simulation with an imposed harmonic roll motion on a cross section. The rotation center is set to be at the center of the square, which coincides with the domain origin. Both the domain and cross section are sharp-angled squares, with wall boundary conditions, as described in subsection 2.4.3. An illustration of the simulation setup is shown in figure 2.6. The roll motion rotates around the geometric center of the square.

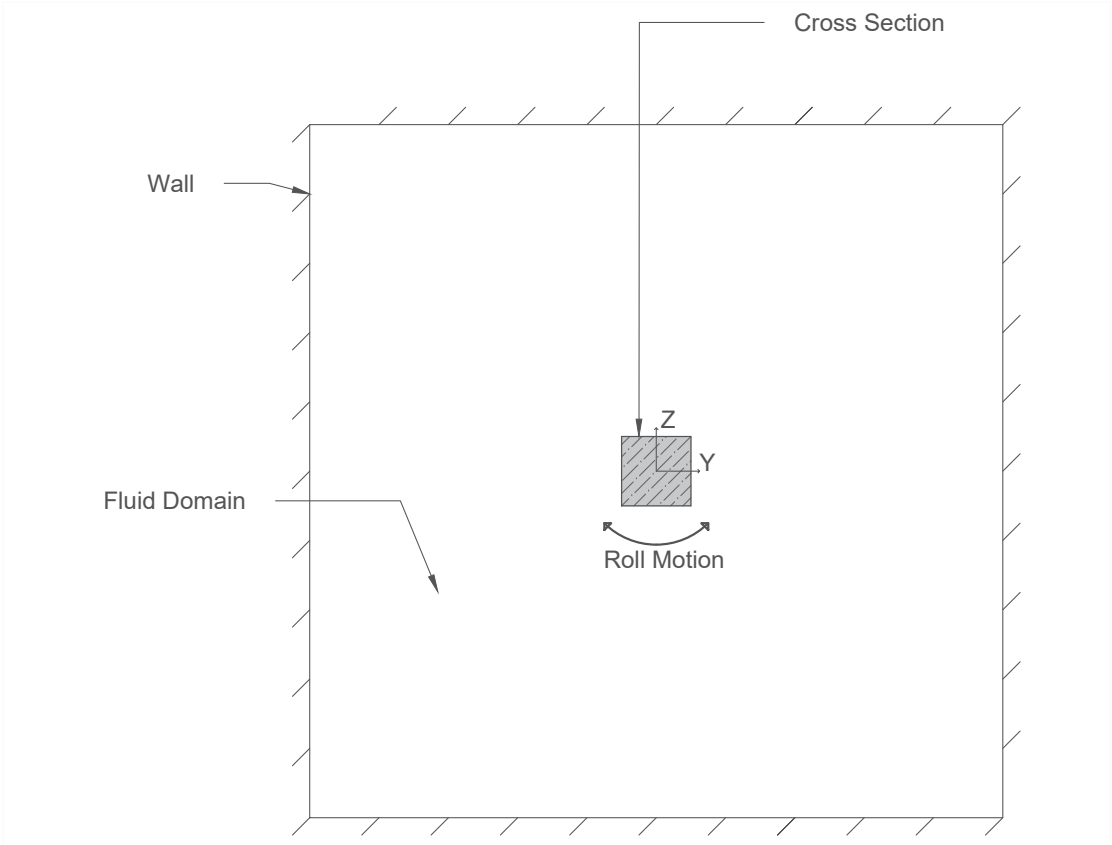

Figure 2.6: Illustration of the submerged simulation setup

The roll moment response from the harmonic motion is recorded, and the added inertia and damping is found using a Fourier transformation for the primary frequency of the imposed motion. This post-processing calculation is more closely described in section 2.7. Unlike free surface simulations, the center of buoyancy for a completely submerged cross section will remain at the geometric center, therefore there is no restoring moment.

The added inertia is compared with the potential theory solution Pettersen (2007):

$$a_{44}^{p} = 0.234\pi\rho B^2 \tag{2.9}$$

2.5.2 Free Surface Simulations

The free surface simulations places the cross sections at the origin, with a draft of half the height. The domain has two boundary conditions, with an upstream (left side) velocity inlet and pressure outlets at the domains downstream side, bottom and top, this is illustrated in figure 2.7. The initial free surface is set to be at z=0 by use of a user field function as described in subsection 2.4.1. The free surface user field function is also enforced on the boundary conditions, such that positions above z=0 only allow air flow through the boundary, while submerged parts of the boundary condition only allows water to flow through the boundary. The domain is 10 meters wide and 4 meters high. The cross section is placed at the origin. The domain top border is at z=1m while the bottom is at z=-3m.

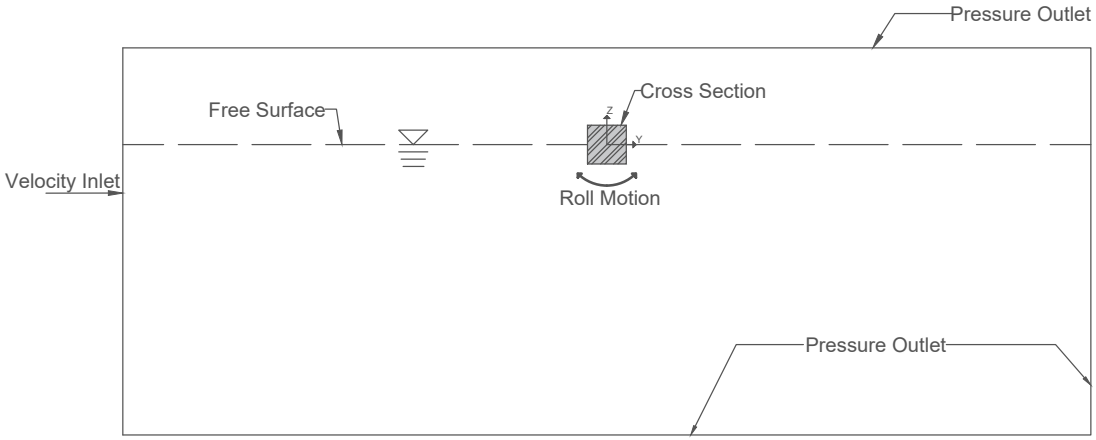

Figure 2.7: Illustration of the free surface simulation setup

The roll moment and sway force are measured for every time step, and the hydrodynamic coefficients are found as described in section 2.7. In order to calculate the linear wave-damping

term, the radiating wave amplitudes are measured by finding the maximum z-position of the free surface both upstream and downstream from the cross section. The free surface that's within 1.3 meters of the cross section is discarded when finding the amplitude, such that the wave amplitude more closely reflects the far-field amplitude. The center of rotation is set to be at the center of the cross section which coincides with the domain origin.

In order to compare the results with experimentally obtained values, both geometries of 2.5mm and 50mm radii is simulated, in addition to several bilge keel designs.

2.5.3 Wave Response Simulations

The simulation setup for wave response is similar to free surface imposed motion simulations, with upstream velocity inlet and a pressure outlet downstream and at the top of the domain. However, the bottom of the domain applies a wall boundary condition instead of a pressure outlet. The pressure and velocity fields applied to the boundary conditions are based on a deep water velocity potential function, as described in subsection 2.4.6. The response is modeled using a Dynamic Body Fluid Interaction (DFBI) motion, which solves the equations for rigid body motion for predefined degrees of freedom. For this thesis only roll motion is enabled.

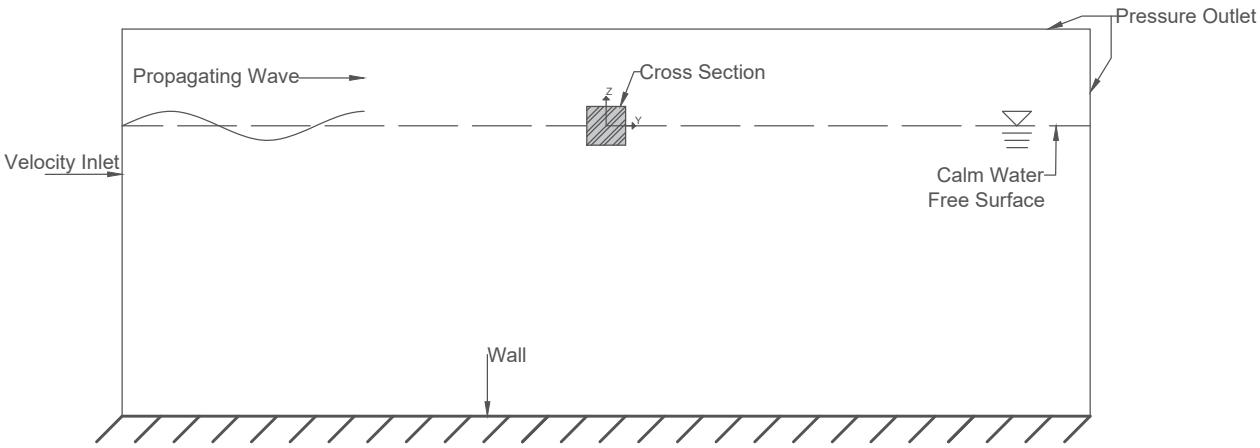

Figure 2.8: Illustration of the wave response simulation setup

Both an 2.5mm corner radius and a bilge keel cross section is used. The bilge keel geometry is described in chapter 2.3.1. Unlike the imposed motion simulations, the wave response rolls around the metacentre. The metacentric height varies depending upon the roll angle, however, for angles less than 10 degrees it is fair to approximate the metacentre to be constant (J. Amdahl,

2015). The meta centric height is given as:

$$GM = KB + BM - KG \tag{2.10}$$

The keel-buoyancy center (KB) is assumed to be half the draft, buoyancy-metacenter distance (BM) is calculated by approximating the cross section as a square of unit length and the keel-gravity center distance (KG) is defined to be 0.12 meters. The resulting metacentric height is thus $GM = 0.04667$ meters. From this the location of the metacenter is defined as the center of rotation.

2.6 Mesh

STAR-CCM+ has an extensive mesh generation features built into the software which is used to generate the mesh. The meshes uses polygon-cells with overset regions to account for the motion of objects within the domains.

The simulations are exclusively two-dimensional, and there are two approaches to simulating two-dimensional flow within STAR-CCM+:

- Create a three dimensional mesh which is 1 cell thick in the z-direction and define boundary conditions of the planes parallel to the xy-plane as "symmetry planes"
- Use the built-in two-dimensional meshing tool which creates a similar mesh that the STAR-CCM+ solvers consider "real two-dimensional mesh"

The advantage of using the built-in approach, is that the resulting mesh is significantly more computationally efficient and therefore is considerably quicker which allows for a higher mesh resolution and cell density [SIEMENS (2017)]. The disadvantage of using the built-in approach, is that several physics continua modules (such as the volume-of-fluid wave module) does not support two-dimensional meshes. For this thesis, the built in module is consistently used.

2.6.1 Overset Meshing

In order to simulate movement of the cross section two meshes are generated; a background mesh and an overset mesh. The background mesh is a static mesh which encloses the entire domain, while the overset mesh encapsulates the cross section and is moving according to the motion of the cross section during the simulation [SIEMENS (2017)]. Within the region of the overset mesh the cells are categorized into three types:

1. **Active cells:** cells in which the discretized governing equations (RANS) are solved.
2. **Inactive cells:** cells from the background region "behind" the overset mesh where no equations are solved.
3. **Acceptor cells:** cells which separate active and inactive cells in the background region,

The acceptor cells acts as a coupling between the two meshes, and values are linearly interpolated between the two meshes.

2.6.2 Boundary Layer Meshing

STAR-CCM+'s prism meshing feature generates layers of quadrilaterals mesh cells normal to "wall" boundaries (see section 2.4). This prism layer is defined in terms of thickness, number of

cell layers, size distribution of the cells and the function which distributes cells. An illustration of such a mesh is found in figure 2.9.

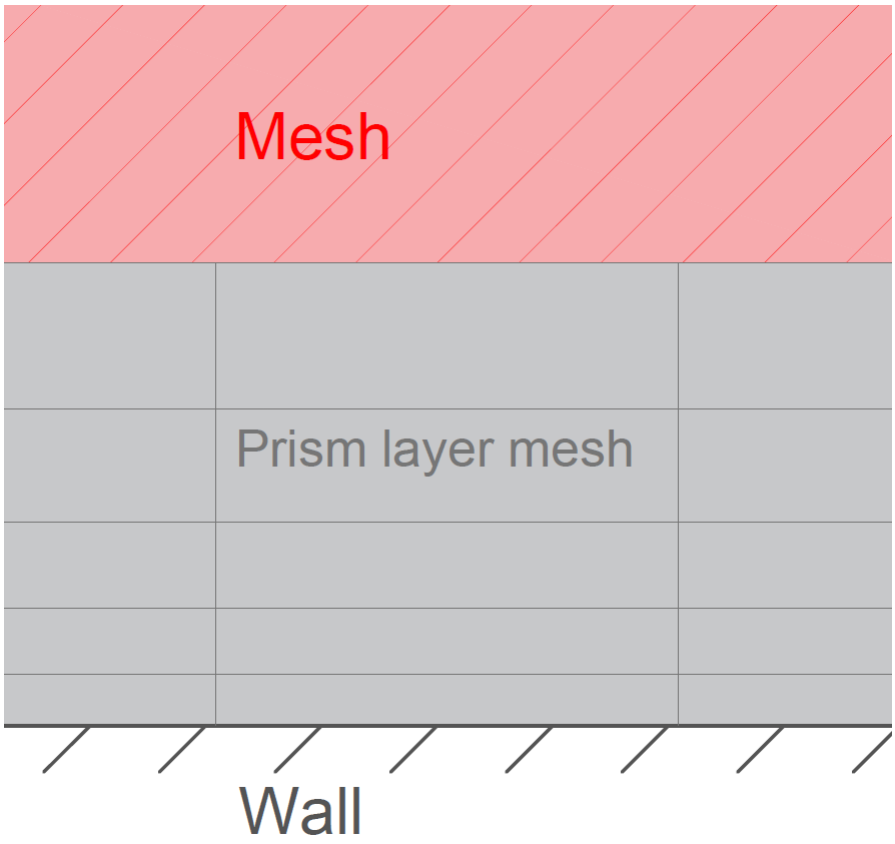

Figure 2.9: An illustration of a prism layer mesh with geometric cell size distribution, 5 cell layers and a stretching factor of 1.3

For all simulations in this thesis the thickness is set to be 5 mm and a geometric cell size distribution is applied. The stretching factor and number of cell layers is adjusted such that the ratio of cell size between the mesh cells outside the prism layer to the outermost layer in the prism mesh is constant (0.2). The outermost cell size is derived from the sum of a geometric series and given by

$$x_n = t\left[\frac{(s-1)s^{n-1}}{s^{n+1}-1}\right] \tag{2.11}$$

where x is cell size, n is number of cell layers, s is the stretch factor and t is the total prism thickness.

A close up of a prism mesh is seen in figure 2.10

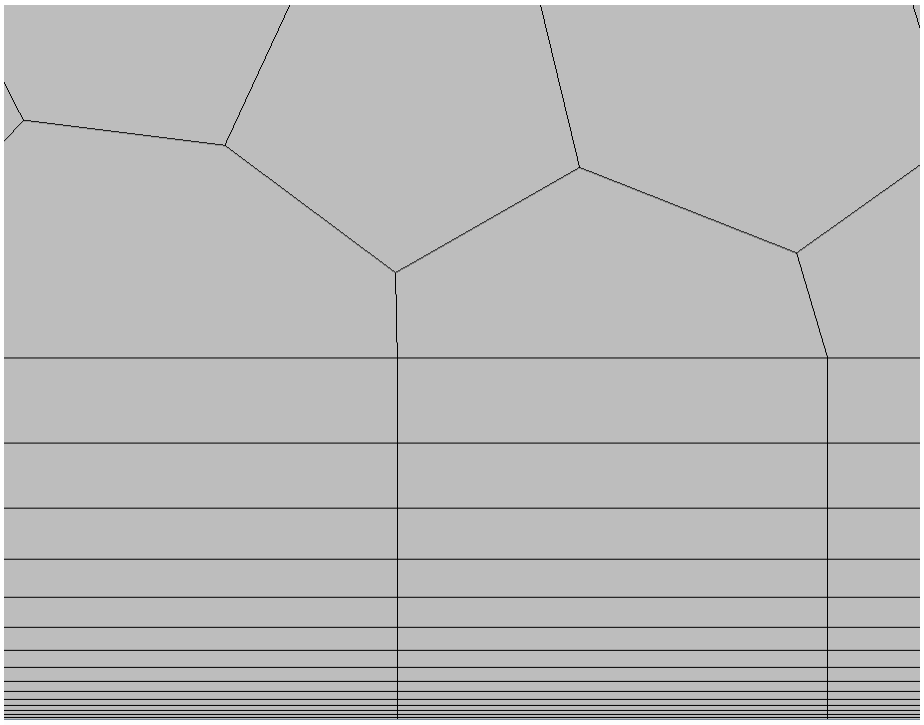

Figure 2.10: A close up picture of the prism layer for a medium mesh density

2.6.3 Meshing of Fully Submerged Simulations

For the simulations of fully submerged geometry the built-in two dimensional mesh generation is applied. The domain is defined as a square with side lengths 10 times longer that the width/height of the cross section. The domain has a cell size equal to the overset edge cell size near/behind the overset region, while the rest of the domain has larger cells/less cell density in order to save computational time. Near the hull a prism mesh generator is applied as described in section 2.6.2.

2.6.4 Meshing of Free Surface Simulations

A rectangular domain with a width of 10 meters and a height of 4 meters is applied. The overset mesh is a square with side length of 0.7m centered at the cross section. The overset mesh has a base size that's 4% of the domain base cell size. Similar to the submerged simulations, the mesh near/behind the overset region is of equal size as the base cell size in the overset region.

It is expected that there will occur flow separation effects near the hull as harmonic motion is applied to the cross section. In order to capture this flow more accurately the cell size is set to be 0.6% of the domain base cell size in this area.

To accurately define the free surface a high mesh resolution is required. This is due to the

free surface being derived from the volume fraction of the cells. Therefore from z = -0.075 to 0.075 the cell size is 1% of the base cell size. In figure 2.11 a picture of a medium-course mesh is shown, with arrows representing the different regions of refinement.

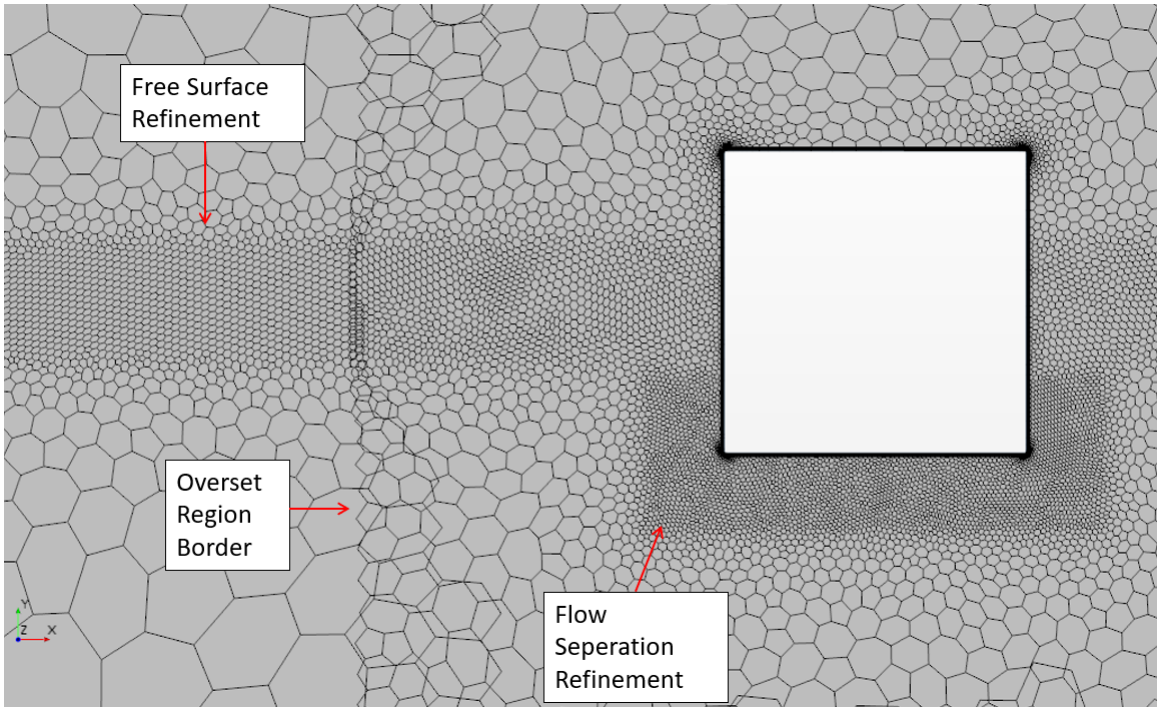

Figure 2.11: The mesh in the overset region of a medium-course mesh, with the different area's of refinement highlighted

2.6.5 Mesh Convergence

In order to preform a mesh convergence test all parameters are defined according to a base size, as described in the subsections above. The mesh convergence is executed by conducting imposed motion simulations on a free surface domain for 3 different base sizes. The resulting roll moment series are analyzed in order to find the hydrodynamic coefficients, as described in section 2.7.

2.7 Calculation of Hydrodynamic Coefficients

To calculate the hydrodynamic coefficients of a cross section an imposed harmonic motion is applied, and the resulting force is found by integrating the pressure on the cross section surface. The harmonic motion is on the form:

$$\eta(t) = \eta_a sin(\omega t) \tag{2.12}$$

where t is time, η_a is the roll amplitude and ω is the frequency.

The imposed harmonic motion is implemented in STAR-CCM+ by defining the rate of rotation (angular velocity) of a reference frame which the overset mesh is set to follow. Centre of rotation is set to be at the centre of the cross section and the rotational axis is normal to the cross section. The rate of rotation is found by derivation of the harmonic motion:

$$\dot{\eta}_4 = \omega \eta_a cos(\omega t) \tag{2.13}$$

The resulting moment from such an imposed motion can be described as the sum of inertia, linearized damping and restoring moments on the form:

$$-a_{44}\ddot{\eta}_4(t) - b_{44}\dot{\eta}_4(t) - c_{44}\eta_4 = M_4(t) \tag{2.14}$$

2.7.1 Restoring Moment

To calculate the hydrodynamic coefficients, the restoring moment needs to be accounted for and removed from the force time series. The restoring moment is found analytically as:

$$M_{restoring} = c_{44}\eta_4 = \forall d\rho g GZ \tag{2.15}$$

where $\forall$ is the cross sectional submerged area, d is the length of extrusion in the z direction, ρ is the water density, g is the gravitational acceleration and GZ is the distance from the centre of buoyancy and centre of rotation.

As the roll angle increases the y-position of the centre of buoyancy relative to the centre of rotation will slightly shift which induces the restoring moment. Since the center of rotation is constant, the moment arm can be found analytically as the geometric centre of the submerged area (beneath the x-axis) of a rotated cross section. This is illustrated in figure 2.12

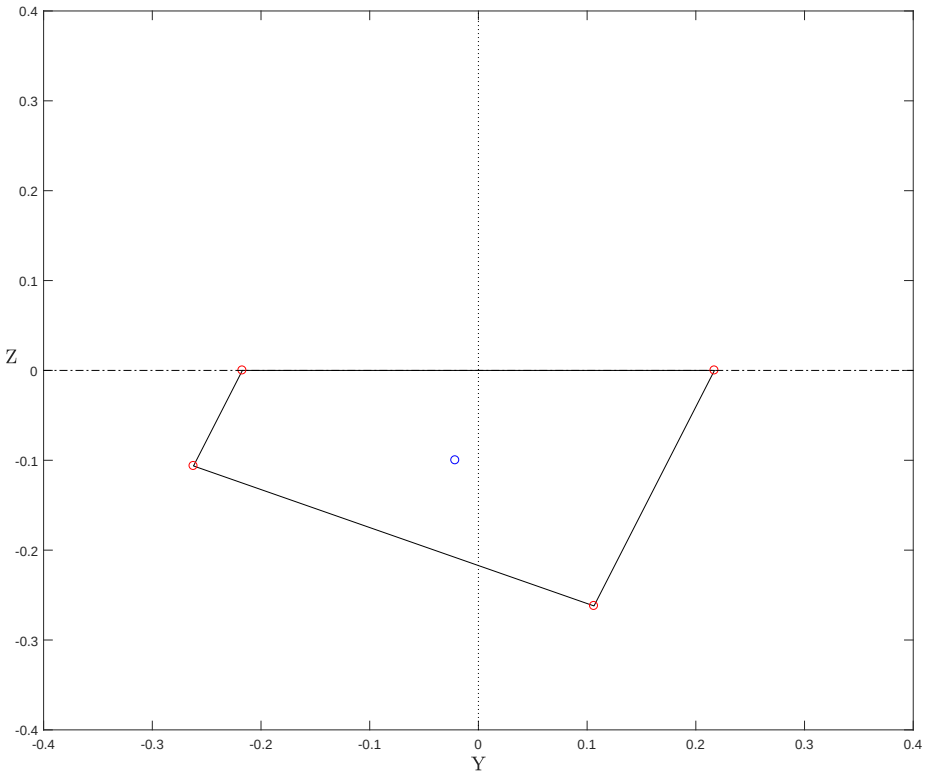

Figure 2.12: An illustration of the shift in centre of buoyancy y-position due to rotation with the center of buoyancy marked in blue and corner vertices marked in red

The geometric center is found by considering the rotated submerged area a polygon with 4 vertices, as marked in figure 2.12. The y-position of the polygons geometric center is then given:

$$Y_b = \frac{1}{6A} \sum_{i=0}^{n-1} (y_i + y_{i+1})(y_i z_{i+1} - y_{i+1} z_i) \tag{2.16}$$

where the vertices of the polygon is given by $(y_1, z_1), ..., (y_n, z_n)$ and A is the polygon's signed area, which due to symmetry corresponds to the submerged area $\forall$ for all angles less than 45 degrees.

For cross sections with 2.5mm corner radius, it is a fair approximation to represent the rotated submerged area with only 4 vertices. However, for cross sections with larger radii this approximation is not accurate. Therefore, the bottom corners for cross sections with 50mm corner radii 5 vertices are place along each bottom corner curves in order to more accurately calculate the GZ distance. The MATLAB code that executes the calculation can be found in appendix D. The effect of bilge keels on hydrostatic forces is neglected.

2.7.2 Calculation of Hydrodynamic Coefficients by Fourier Analysis

Once the restoring moment is calculated the moment induced by the harmonic motion can be expressed as:

$$-a_{44}\ddot{\eta}_4(t) - b_{44}\dot{\eta}_4(t) = M_4(t) + M_{restoring} = \hat{M}_4(t) \tag{2.17}$$

where a_{44} is the added inertia coefficient in roll, b_{44} damping coefficient and $M_4(t)$ is the resulting moment series from the simulation. The instantaneous added inertia and damping coefficients are found by extracting the Fourier coefficient of the primary frequency over a period T for a point in time t_0:

$$a_{44}(t_0) = \frac{1}{\pi\eta_{a,44}\omega}\int_{t_0-T/2}^{t_0+T/2} \hat{M}_4(t)\sin(\omega t)\,dt \tag{2.18}$$

$$b_{44}(t_0) = -\frac{1}{\pi\eta_{a,44}}\int_{t_0-T/2}^{t_0+T/2} \hat{M}_4(t)\cos(\omega t)\,dt \tag{2.19}$$

By evaluating the time series for sway forces, X_2, instead of roll moment, the coupled sway-roll coefficients can be found by the similar approach. However, since there is no restoring sway force there is no need to alter the force time series. Therefore the coupled coefficients can be calculated for a point in time t_0 as:

$$a_{24}(t_0) = \frac{1}{\pi\eta_{a,44}\omega}\int_{t_0-T/2}^{t_0+T/2} X_2(t)\sin(\omega t)\,dt \tag{2.20}$$

$$b_{24}(t_0) = -\frac{1}{\pi\eta_{a,44}}\int_{t_0-T/2}^{t_0+T/2} X_2(t)\cos(\omega t)\,dt \tag{2.21}$$

These instantaneous coefficients are averaged over time in order to get steady state coefficients. In order to compare the coefficients and frequency with other work, they are made dimensionless as follows:

$$a_{44}^* = \frac{a_{44}}{\rho\forall B^2} \tag{2.22}$$

$$b_{44}^* = \frac{b_{44}}{\rho\forall B^2}\sqrt{\frac{B}{2g}} \tag{2.23}$$

$$a_{24}^* = \frac{a_{44}}{\rho\forall B} \tag{2.24}$$

$$b_{24}^* = \frac{b_{44}}{\rho\forall B}\sqrt{\frac{B}{2g}} \tag{2.25}$$

$$\omega^* = \omega\sqrt{\frac{B}{2g}} \tag{2.26}$$

where B is the beam width of the cross section. The MATLAB code computes the integrals can be found in appendix D.

2.7.3 Composite modeling of non-linear viscous damping

Equation 2.17 does not include non-linear damping, however for a rolling cross-section damping will have contributions from wave making as well as flow separation. In order to separate the two Yeung et al.'s approach and composite model (first proposed by Yeung et al. (1998)) is applied, in this section a brief explanation of his approach is presented.

By first considering the case for a cross section submerged in infinite fluid, the resulting moment from a harmonic motion can be expressed in terms of the added inertia and quadratic damping:

$$M_q(t) = -a_{44}\ddot{\eta}_{44} - b'_{44}\dot{\eta}_{44}|\dot{\eta}_{44}| \tag{2.27}$$

where b'_{44} represents the quadratic damping coefficient and can be calculated by:

$$b'_{44}(t_0) = \frac{-3}{8\eta^2_{a,44}\omega}\int_{t_0-T/2}^{t_0+T/2} M_4^q(t)\cos(\omega t)\,dt \tag{2.28}$$

Yeung et al.'s composite approach assumes that both wave making damping and flow separation damping is of equal importance and that therefore if equation 2.19 is applied the linear damping term would absorb the non-linear contributions. In order to represent these two damping contributions independently, the linear-damping contribution is assumed to only consist of the radiating waves and the remaining flow separation damping is represented by a quadratic term:

$$M_c(t) = -a_{44}\ddot{\eta}_{44} - b^w_{44}\dot{\eta}_{44} - b^q_{44}\dot{\eta}_{44}|\dot{\eta}_{44}| \tag{2.29}$$

where b^w_{44} is the linear damping coefficient and b^q_{44} is the non-linear coefficient.

These two coefficients are determined uniquely by decomposing the time-averaged mechanical power, $\dot{W}$ into a component corresponding to the radiating waves, $\dot{W}_w$, and one corresponding to the viscous effects, $\dot{W}_q$. The radiating wave term is found by evaluating the amplitudes of far field radiating waves upstream and downstream (A_- and A_+). The time-averaged energy flux of the radiating wave is then given as:

$$\dot{E} = \frac{\rho g^2}{4\pi}\int_{t_0-T/2}^{t_0+T/2} (|A_+|^2 + |A_-|^2)\,dt \tag{2.30}$$

While the rate of work done by the wave making term onto the cross section is represented as:

$$\dot{W}_w = \frac{1}{T}\int_{t_0-T/2}^{t_0+T/2} (b_{44}^w \dot{\eta}_{44})\dot{\eta}_{44}\,dt = \frac{b_{44}^w \eta_0^2 \omega^2}{2} \tag{2.31}$$

Since the time-averaged energy of wave damping is represented by the linear damping term, the rate of work must be equal to the energy flux of the radiating waves, $\dot{W} = \dot{E}$. From this the following expression can be derived for the linear wave-damping coefficient:

$$b_{44}^w = \frac{\rho g^2}{2\pi\eta_0^2\omega^2}\int_{t_0-T/2}^{t_0+T/2} (|A_+|^2 + |A_-|^2)\,dt \tag{2.32}$$

The linear contribution can now be removed from the total moment:

$$M_q^*(t) = M(t) + b_{44}^w \dot{\eta}_{44} = -a_{44}\ddot{\eta}_{44} - b_{44}^q \dot{\eta}_{44}|\dot{\eta}_{44}| \tag{2.33}$$

The quadratic damping can now be found using the traditional approach for infinite fluid damping coefficient in equation 2.28.

One of the advantages of Yeung's composite model is that it quantifies how much damping is due to first and second order damping, and thus is useful for comparison of flow separation damping which is non-linear.

Central to calculation of Yeung's wave-damping coefficient is the determination of wave amplitude. As described in chapter 2.2.3, the free surface is defined from the fluid volume fractions of a cell. The surface elevation is found as the z-position of the free surface, thus by finding the maximum surface elevation the wave amplitude is found. Since the waves of interest is the far-field waves, the area nearest the cross section (within $1.3m = \sim 3$ beam lengths) is disregarded.

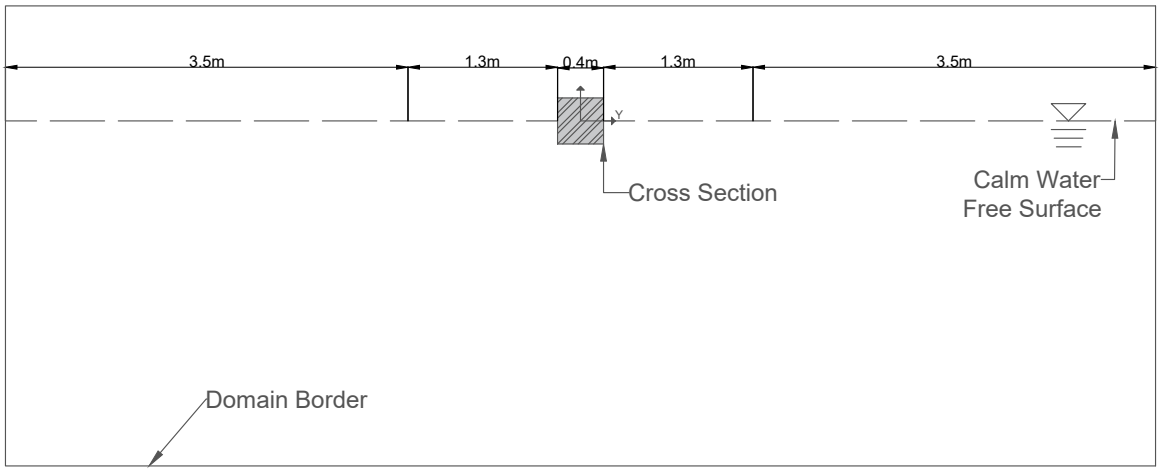

Figure 2.13: Sketch showing the length where the wave amplitude is found

For low frequencies registering the wave amplitude becomes a challenge due to the wave length exceeding the domain size. As described in chapter 2.5.2, the horizontal distance from the origin to the domain boundary is 5 meters. Since the area near the cross section is disregarded, the total length over which the wave-amplitude is found is 3.5 meters (both upstream and downstream), see figure 2.13.

We assume that the radiating waves act as potential theory waves at infinite water depth, the wave length is given by the equation:

$$\lambda = \frac{g}{2\pi}\left(\frac{2\pi}{\omega}\right)^2 \tag{2.34}$$

In order for the wave amplitude to be found for all time instances the wave length must be shorter than the length over which it is found. Hence, for the composite model can only be applied for frequencies higher than $\omega =\sim 4.2[rad/s]$.

A possible remedy that enables the composite model to be applied for low frequencies, is to increase the domain length. However, this increases the computational cost required.

The MATLAB code that computes the integrals can be found in appendix D.

Chapter 3

Quality Analysis

3.1 Time Convergence

In figure 3.1 the roll moment time series of varying time-step is plotted.

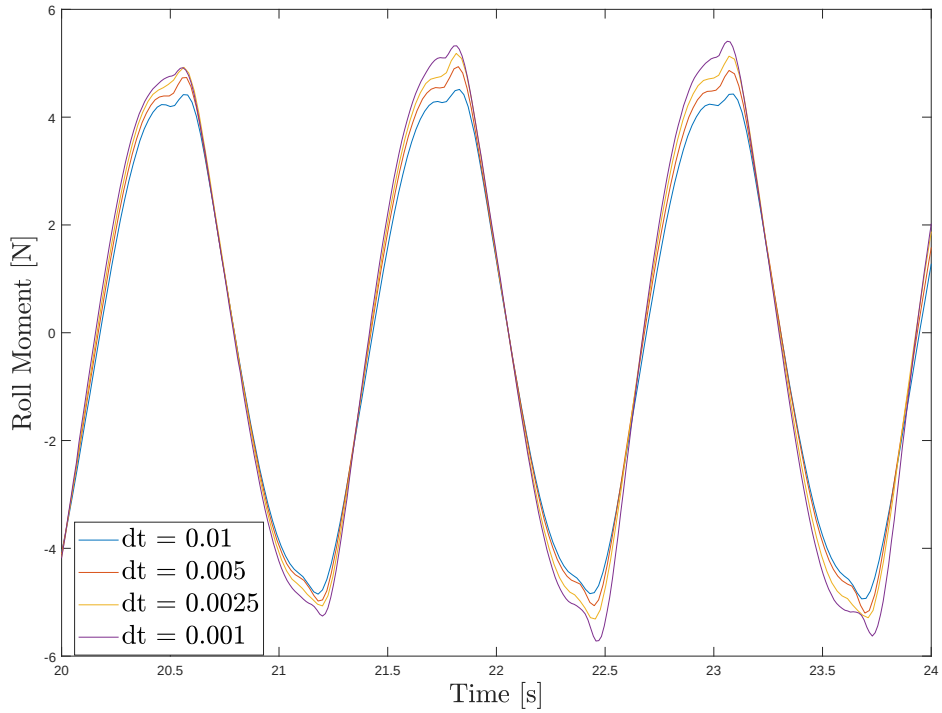

Figure 3.1: Response roll moment time series with frequency $\omega^* = 0.7139[-]$ for varying time-steps (dt)

All the moment series plotted in figure 3.1 has the same frequency, mesh resolution and

inner iterations per step (20). The time series appears to show an increase in moment amplitude for lower time-steps in addition to a more pronounced non-linearity. The flow at the time shown in figure 3.1 is however still transient and for more developed flows the difference is not clearly seen from moment time series. A perhaps better approach to evaluating the time convergence is inspecting the change in hydrodynamic coefficients for different time-step lengths. The added inertia and linear-model damping is calculated as described in section 2.7.

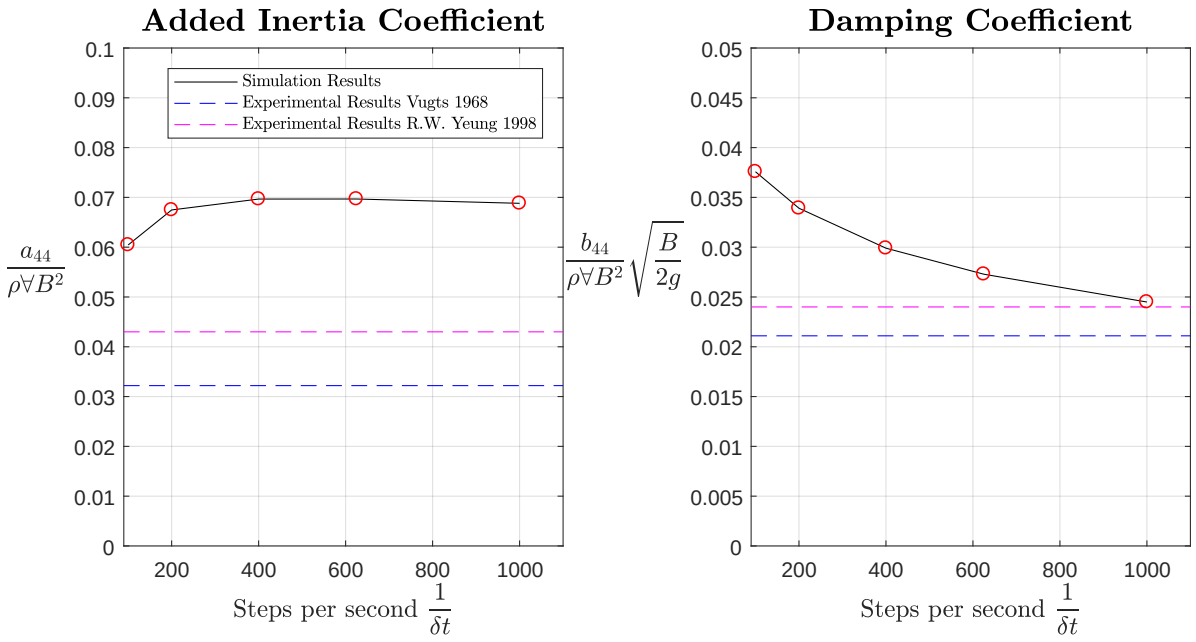

Figure 3.2: Hydrodynamic coefficients plotted against number of time-step per second. Compared to experimental results from Vugts (Vugts, 1968) and R.W Yeung (Yeung et al., 1998). The coefficients are calculated over the time range 40-60 seconds.

Added roll inertia converges towards a value of $a_{44}^* = 0.0635$, this is significantly higher than the experimental values found by both Vugts (1968) and Yeung et al. (1998). In passing, we note that a study conducted by Quérard et al. (2009) reports similar added roll inertia values for a range of time-steps and equivalent RANS simulations. Quérard, unlike this thesis, applies a SST $k-\omega$ turbulence model and a quadrilateral mesh cells, which implies that the disparity between the calculated and experimental results is not due to mesh refinement nor time-step size. The damping coefficient appears to be converging towards the experimental values, yet it is not possible to see from the graph whether or not the finest time-step resolution is adequately small to be considered converged. However, due to the computational time required, additional simulations with lower time-step than 0.001 seconds (1 ms) is not conducted.

3.2 Mesh Convergence

The mesh convergence is conducted with a constant time-step of 0.001 seconds. Due to computational constraints the finest mesh is only run for 47.61 seconds, unlike the 60 seconds convention in this thesis. Therefore, the time range upon which the coefficients are calculated is from 36 seconds onwards. The impact of this is limited, as seen in the middle value which corresponds to base cell of 1, which is the same simulation as used for the finest time-step convergence. The damping values for this coefficient is approximately the same for both time ranges. In figure 3.3 the convergence curve for the linearized damping is presented.

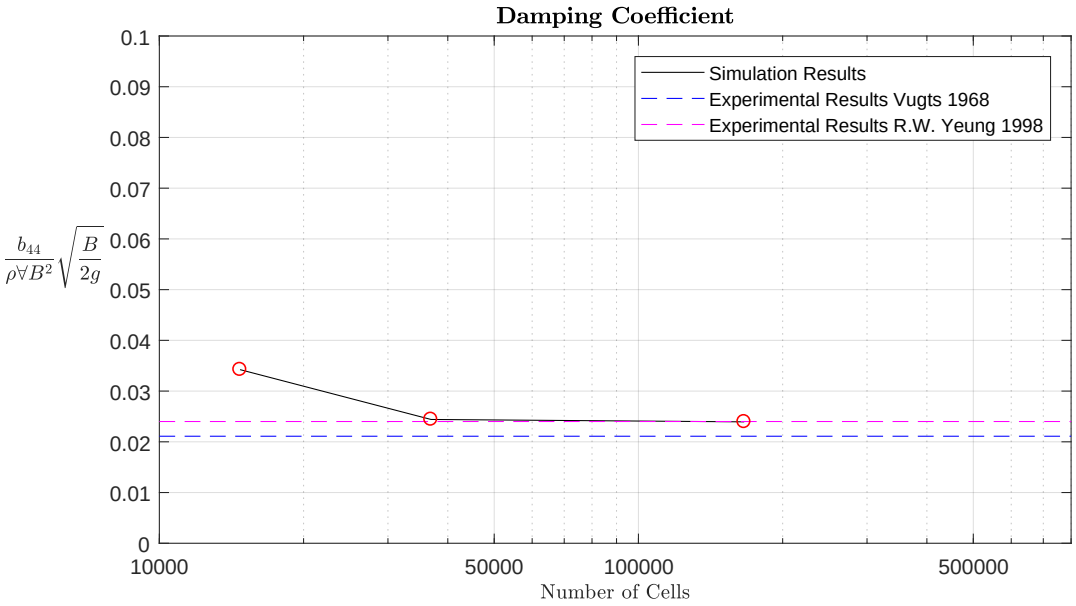

Figure 3.3: The mesh convergence plot for linearized damping

The mesh appears to converge towards the experimental results, with little gain after~ 36900 cells.

Yeung's composite model is dependent upon accurately capturing the outgoing amplitude of the far-field waves radiating from the cross section. The amplitude of the mesh is of course derived from the free surface, which again is calculated from the volume-of-fluid fraction for each individual mesh cell. Thus is the accuracy of predicting the wave-damping mesh dependent. In figure 3.4 a convergence curve for the wave-making damping coefficient is shown.

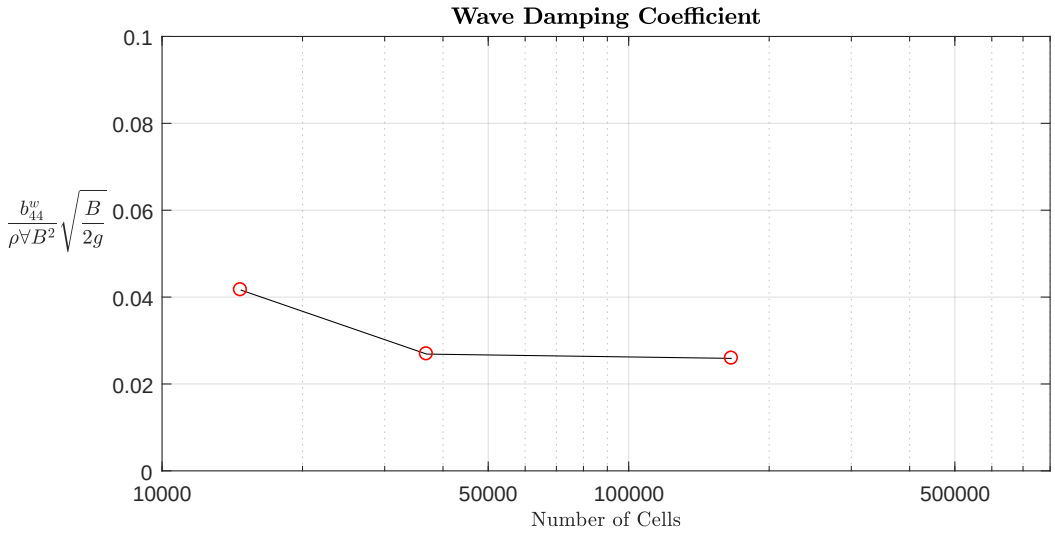

Figure 3.4: Wave-damping coefficient plotted against mesh cell count

The wave making appears to have converged for a cell count of ~ 36900. However, for wave-making simulations it is very important to solve the surface elevation accurately for the wave motion to be simulated correctly. Therefore, harmonic motion simulations utilize meshes with ~ 36900 (which corresponds to a base size of 1), while wave-response simulations utilizes a mesh ~ 166000 (which corresponds to a base size of 0.5).

3.3 Low Frequency Challenges

There are inherent challenges in measuring the hydrodynamic forces acting at low frequencies due to the linear and non-linear frequency proportionality of the forces. As discussed in chapter 2.1, for oscillating motion the magnitude of velocity is proportional to frequency. Similarly acceleration amplitude is proportional to frequency squared. In terms of amplitude magnitude stiffness has no proportionality. Therefore, at low frequencies the inertia and damping terms become very small, and stiffness dominates.

Small force terms means that the impact of other error sources, such as noise for experiments or numerical precision in CFD simulations, has a larger impact on the calculations. An example of this is the experimentally obtained added inertia found by Vugts (1968), which found a negative added inertia for the lowest frequency tested ($\omega\sqrt{\frac{B}{2g}} = 0.2$). A scan of the experimental results is shown in appendix B.

Added inertia, in particular, becomes very sensitive to accounting of the restoring moment since both harmonic motions are sine functions for small angles. At higher frequencies, the inertia term grows significantly which reduces the impact of inaccuracy in calculating the restoring moment.

For wave response simulations low frequencies induces additional complications. Due to the potential function used to simulate waves being a deep water velocity potential and the bottom boundary condition being a wall, there are limitations of how long waves the domain can accurately simulate. Deep water waves dies out exponentially according to the e^{kz} term in the velocity potential. Low frequencies has low wave numbers (k), which reduces the rate of decay. If we assume that once the e^{kz} is less than 0.05 at the domain bottom ($z = -3$) for the effects to be negligible, the wave number must be above 1. The bottom limit frequency can be found from the equation for wave number; $k = \frac{\omega^2}{g}$. Imposing the requirement $k \leq 1$, the lowest wave frequency allowed becomes $\omega \approx 3.1[rad/s]$.

Chapter 4

Results

4.1 Imposed Harmonic Motion

4.1.1 Fully Submerged Simulations

As described in chapter 2.5.1, a square with sharp corners is forced to roll with a harmonic motion and the roll moment response is measured. The added inertia is found as described in chapter 2.7. Since the cross section is fully submerged, there is no restoring moment. In table 4.1 the resulting added inertia presented along with added inertia calculated from potential theory (Pettersen, 2007).

Table 4.1: Added inertia calculated from CFD simulation and Potential Theory

	Computed From CFD	Potential Theory
a_{44}	23.38 $[kg \cdot m]$	18.82 $[kg \cdot m]$
$\frac{a_{44}}{\rho \forall B^2}$	0.91 [-]	0.74 [-]
b_{44}	70.1 $[[kg \cdot m/s]$	-
$\frac{b_{44}}{\rho \forall B^2}\sqrt{\frac{B}{2g}}$	0.39 [-]	-

The added inertia is slightly higher than the potential theory. There is limited experimental data available for comparison, we note however, that for experiments on rolling rectangular cylinders in the free surface the inviscid solutions tend to overestimate the added inertia slightly (Vugts (1968),Yeung et al. (1998),Yeung et al. (2001)).

4.1.2 Free Surface Simulations

In order to inspect the damping-frequency relationship, a range of frequencies needs to be inspected. At a time-step of $\delta t = 0.001s$, the computational time required would exceed what was

available. As a compromise the time step is reduced, in order to compensate for the loss of accuracy the inner iterations is increased. Two different time-steps are simulated ($\delta t = 0.01s$ and $\delta t = 0.03s$), both with 100 inner iterations. Compared to the $\delta t = 0.001s$ simulation conducted in time-convergence test, the total iterations required is reduced by 50% and 83%. The simulations are run with frequencies $\omega = 1,2,3..,10[rad/s]$. Resulting hydrodynamic coefficients are shown in figure 4.1:

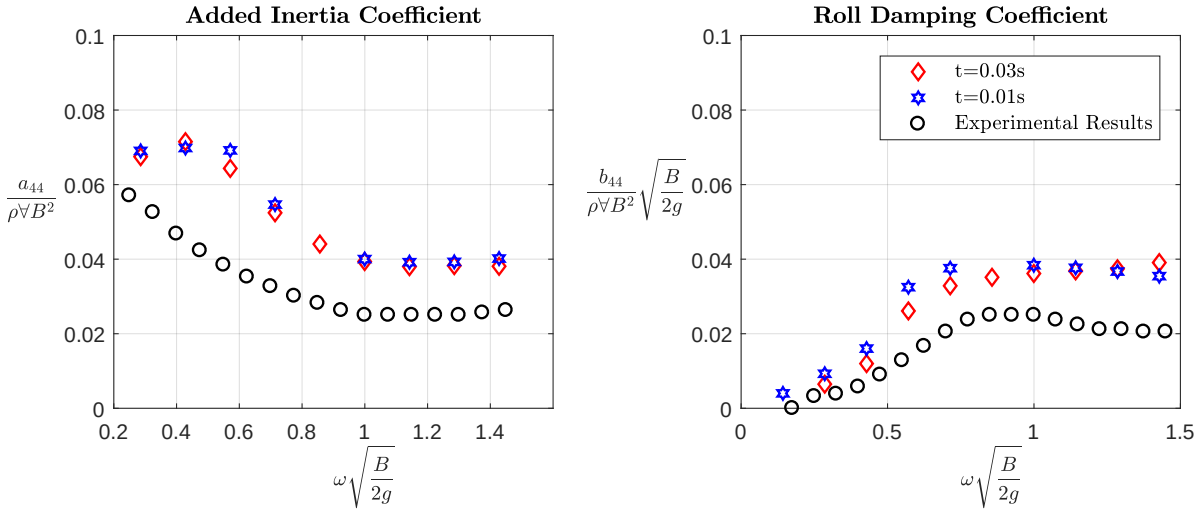

Figure 4.1: Hydrodynamic coefficients for simulations with time-step of 10 and 30 ms. Experimental values from Vugts (Vugts (1968))

Both damping and added inertia coefficients for $\delta t = 0.01s$ is continually higher than the experimental results, with no clear improvements compared to the time-convergence test with 20 inner iterations. However, the difference between $\delta t = 0.01s$ and $\delta t = 0.03s$ is marginal compared to the significant amount of computational time that is saved. Despite showing a significant overestimation of damping, the general form of the damping is represented with both time-steps; damping approaching zero at low values, peak values near $\omega^* = 0.75[-]$ and a stabilization at high frequencies. It is therefore the author's belief that this will also be the case for similar two-dimensional geometries. Therefore additional simulations that is intended to capture the development over a range of frequencies utilizes a time-step of $\delta t = 0.03s$.

Coupled Coefficients

The coupled terms in sway-roll are found from the sway force time series from the imposed motion simulation, as described in chapter 2.7.2. The in figure 4.2 the coupled roll-sway added mass and damping is shown for a spectrum of frequencies. The simulation used to calculate the coupled coefficients is the same for the uncoupled.

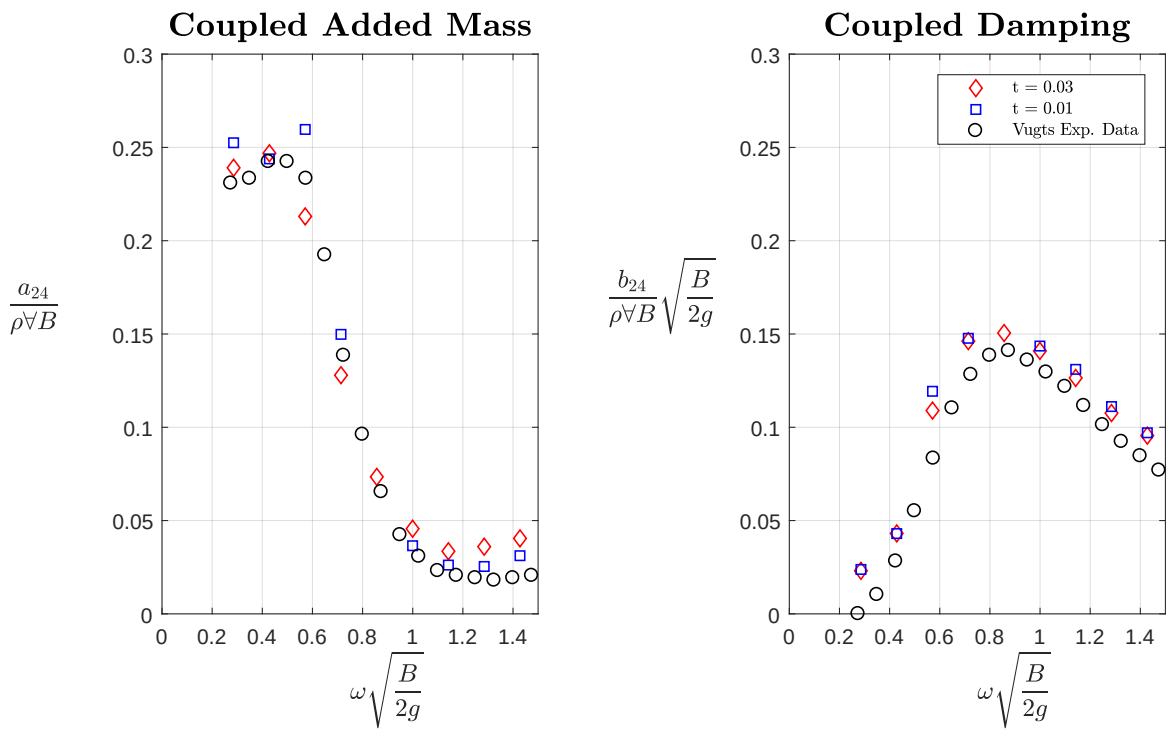

Figure 4.2: The coupled hydrodynamic coefficients for a cross section with 2.5mm corner radius

The coupled coefficients show good agreement with the experimental results found by Vugts (1968). It is of note that experiments conducted by Yeung et al. (1998) reports a lower low frequency added inertia values than Vugts. The damping coefficient is consistent from both experiments.

4.1.3 Comparison of Cross Section Geometries

In figure 4.3 a comparison of the hydrodynamic coefficients for the two different corner radius is shown (see chapter 2.3). The simulations utilizes a time-step of $\delta t = 0.03s$ and the coefficients are calculated from 40-60 seconds into the simulation.

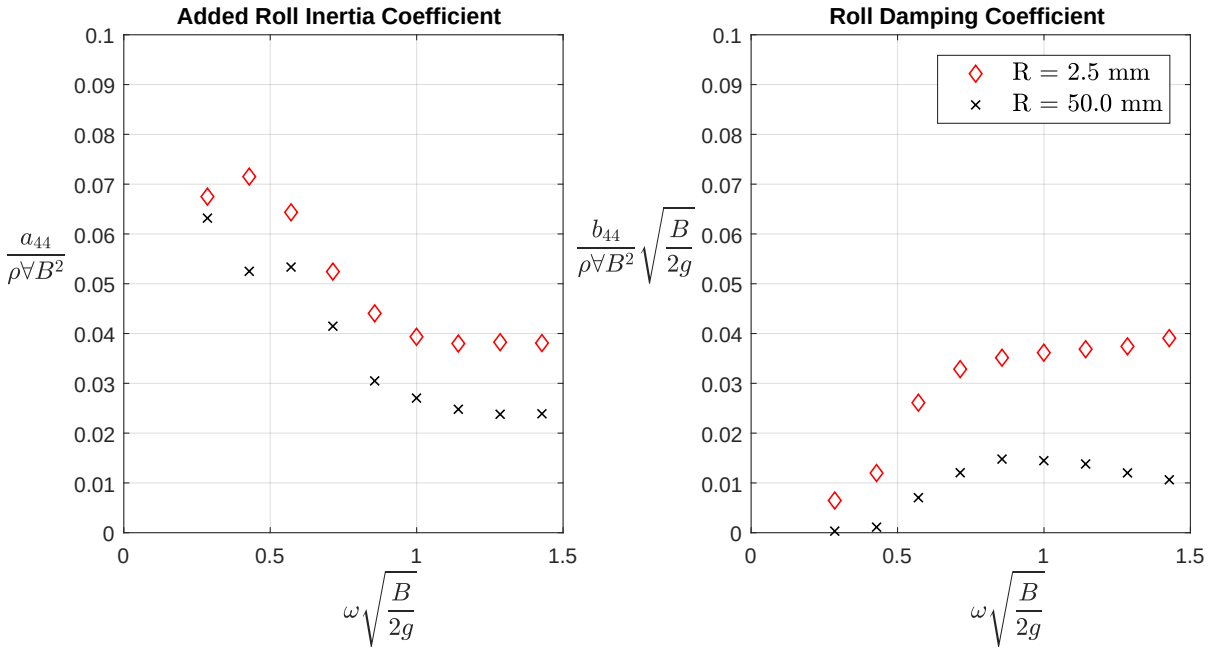

Figure 4.3: Comparison of hydrodynamic coefficients for geometries of different corner radius

From the results a higher corner radii exhibits lower damping and added inertia. If the simulation behavior of overestimation compared to experimental values is also true for the larger corner radius geometry, the true values are even lower. It is of interest to know to which degree the reduction of damping is due to reduction in wave-making or flow separation effects. To that end, the wave damping coefficient is found according to Yeung's approach (see section 2.7.3, eq. 2.32). The resulting coefficients for the two different cross sections are shown in figure 4.4.

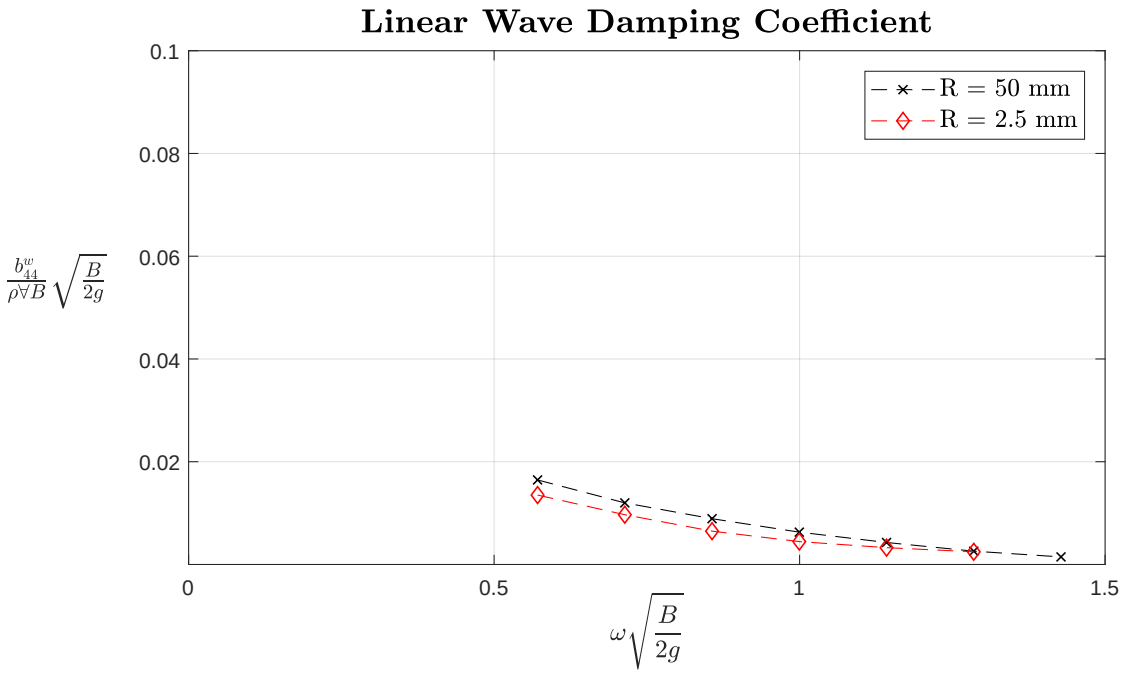

Figure 4.4: Comparison of the wave making damping coefficients for different corner radius

As described in chapter 2.7.3, frequencies under $\omega = 4.2$ has too long wave lengths to accurately capture the wave amplitude. Therefore the wave-damping coefficients shown above corresponds to $\omega = 5, 6.., 10$ ($\omega\sqrt{\frac{B}{2g}} = 0.71, 0.86, .., 1.43$).
The figure shows, the wave damping is near equal for both cross sections. It's therefore reasonable to assume that the reduction in damping for a larger corner radius is primarily due to a reduction in flow separation/eddy making damping.

The coefficients must not be confused with the damping moment. From equation 2.14 we note that a linear damping model is expressed as $-b_{44}\dot{\eta}_4(t)$, and as such is proportional to roll velocity. For harmonic motions, the velocity in turn is proportional to frequency (as seen in equation 2.13). Therefore, as the frequency approaches zero the damping moment will approach zero. From figure 4.4, we note that the coefficient is approaching zero for high frequencies. This coincides with previous research (Faltinsen, 1993).

The wave-damping for $\omega = 5$, has a damping that is ~ 6% higher than the damping found from the Fourier coefficient of the primary frequency, as shown in figure 4.3. This results in a negative quadratic damping, which is unphysical. This strongly implies that the wave damping is overestimated. Due to the methodology of finding the wave coefficient depends upon accurately capturing the far-field wave amplitude, the most probable cause of the overestimation is that the free surface elevation is not found accurately enough. This is shown more closely in chapter 3.2.

As discussed above, higher frequencies has a lower wave damping. Therefore, even if the

wave-damping is over estimated it does not exceed the linear damping found from the roll moment time series.

4.2 Impact of Bilge Keel Length

Three different bilge keel lengths are tested, for the hull with large corner radius, as described in chapter 2.3.1. As discussed in chapter 4.1, a time step of $\delta t = 0.03$ is chosen as a compromise between computational time and numerical accuracy. Since the damping was consistently overestimated, we expect that this will be the case for bilge keel fitted geometry as well. However, the damping curve as a function of frequency is expected to have a shape representative of the true damping even if the magnitude is overestimated.

In figure 4.5 the linear damping is found as the Fourier coefficient of the primary frequency (as described in chapter 2.7.2) for different bilge keel lengths is shown. A description of the bilge keel geometry is found in chapter 2.3.1.

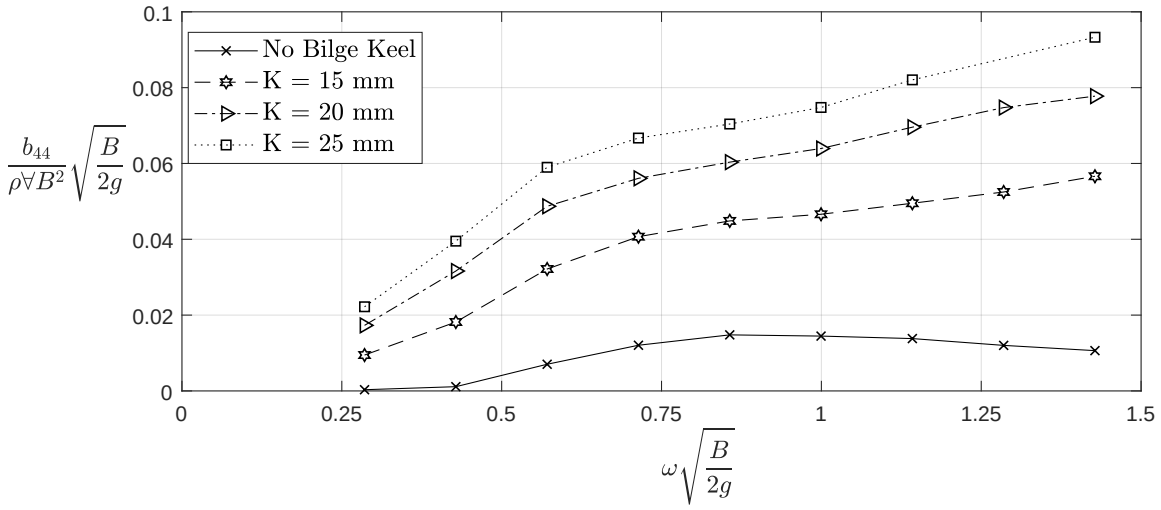

Figure 4.5: The linearized damping for different bilge keel lengths

As expected, bilge keel fitted cross sections show an significant increase in roll damping for all frequencies. While different in magnitude, the general curve shape of the damping is similar for all three bilge keel lengths. Unlike the bare hull cross section, the damping coefficient for bilge keel fitted cross sections is increasing for the entire range of frequencies tested. A possible reason for the contentiously increasing values is that the linear coefficient is accounting for the higher-order components of the damping. As R.W Yeung postulated in his proposal of a composite model:

"Eq. 2.28 is based on equivalent energy dissipation. However, there exists geometry for which both wave-radiation damping and flow-separation damping is of

> equal importance. If Eq. 2.19 is used instead, one expects b_{44} to incorporate the linear equivalent of some non-linear effects on an approximate basis." -Yeung et al. (1998)

Note that, the equation refers to the quadratic and linear damping coefficient integral respectively, and the reference number has been altered to refer to the listing of this thesis. The nomenclature for damping has also been changed to stay consistent with the thesis.

In order to quantify the different sources of damping (wave and second order) that is acting on the cross section for different bilge keel lengths, Yeung's composite model approach is utilized as described in chapter 2.7.3. The resulting coefficients are shown in figure 4.6.

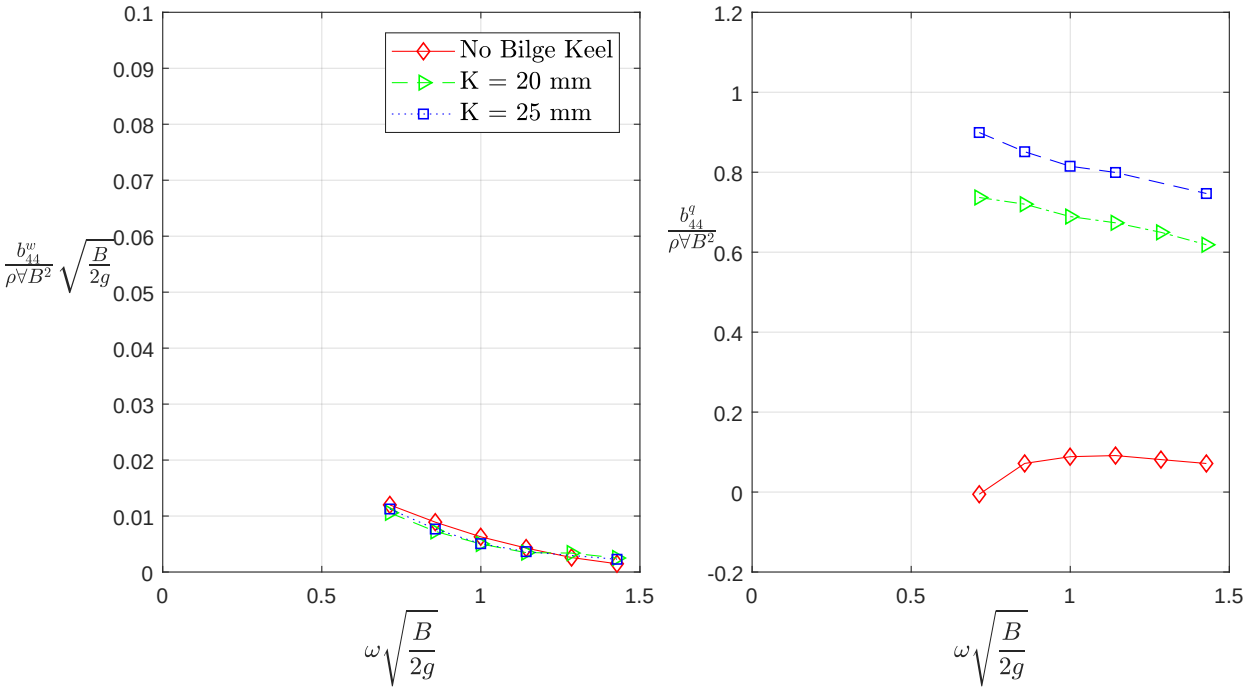

Figure 4.6: The wave-damping coefficient (b^w) and quadratic composite coefficient (b^q) for different bilge keel lengths (K)

Due to an error, the surface elevation for the 15 millimeters was not recorded, and is therefore not presented. As discussed in chapter 2.7.3, Yeungs approach is not applicable for frequencies under $\omega = 4.2$ for the simulated domain size. The wave damping (b^w) for the cross section without bilge keels is overestimated as is apparent from the slightly negative quadratic damping ($b^q = -0.0002$) for $\omega = 5$. However, if we assume that the overestimation of wave-making damping is consistent for all cross sections, we can conclude from the near equal coefficients

as seen in figure 4.6 that the wave damping is near unaffected by the bilge keels. The composite quadratic coefficient is significantly higher for bilge keels.

As described in chapter 2.1, a constant second order coefficient results in a quadratic proportional growth of the second order term. Therefore, the reduction in quadratic coefficients seen in figure 4.6 does not result in a reduction of total quadratic damping moment. This is illustrated in figure 4.7, where the linear and quadratic coefficient is multiplied with the peak harmonic motion velocity ($\eta_{4a}\omega$), and the peak velocity squared. Both a hull without bilge keels, and with maximum length bilge keels is shown. Duo to an error in the setup, there is no surface elevation data from the 15mm bilge keel simulation, and is therefore not inspected by Yeung's composite model.

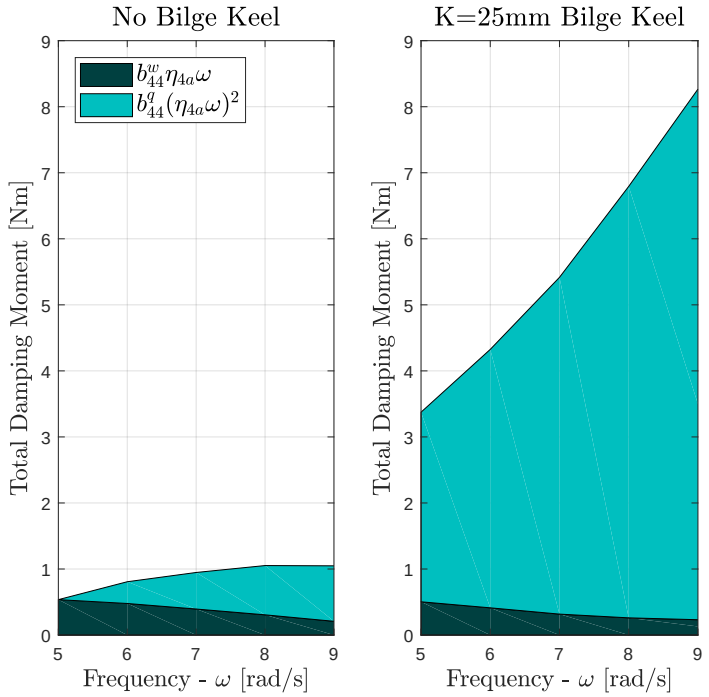

Figure 4.7: The linear and quadratic composition of damping, for a cross section with and without bilge keels

The figures above illustrates that despite a reduction in quadratic damping coefficient at higher frequencies for both cross sections, the quadratic damping term is not decreasing. The graphs are plotted with the same scale, in order to illustrate the significant higher damping that is induced by the bilge keels.

The added inertia due to bilge keels is also calculated and presented in figure 4.8.

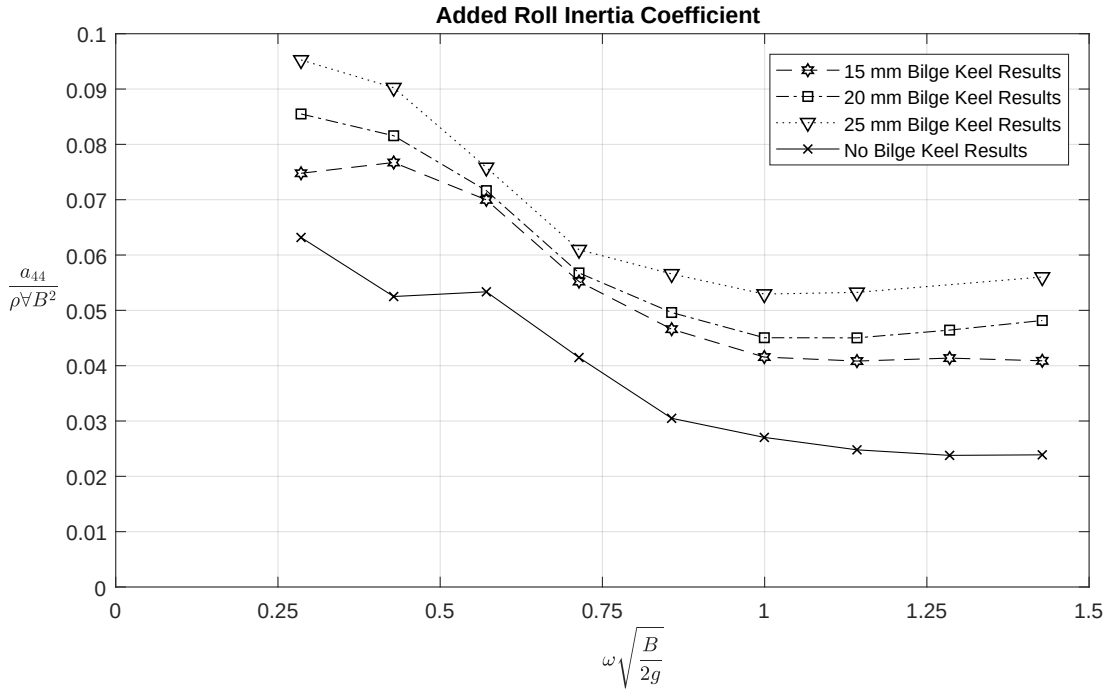

Figure 4.8: The added inertia coefficient for different bilge keel lengths

As with the damping from $dt = 0.03$ time-step simulations, the added inertia values are expected to be overestimated in value, but be similar in form to the true added inertia. Figure 4.8 shows that increasing the bilge keel length increases the added inertia. This is consistent with experimentally and numerically by free-surface random vortex simulations for bilge keels of slightly different geometry but of similar lengths conducted by Yeung et al. (2001).

4.2.1 Impact of Bilge Keel Tip Geometry

An alternative bilge keel tip, as described in chapter 2.3.1, is inspected. In figure 4.9 the two damping coefficient for the two tip shapes are compared.

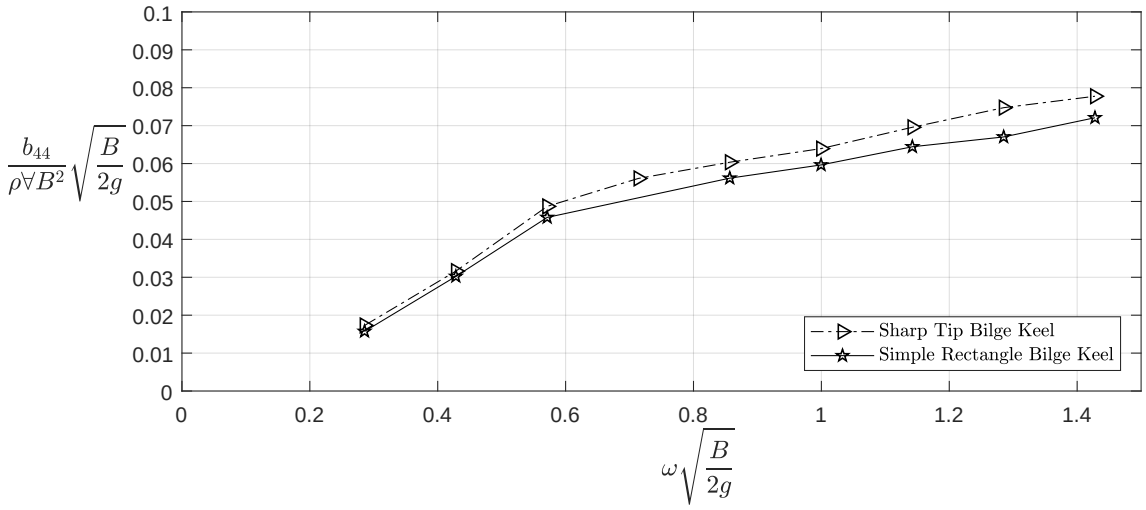

Figure 4.9: Linearized damping coefficient for bilge keels different tips, but equal length (K = 20.76mm)

The rectangular bilge keel appears to outperform the sharp bilge keel, especially at higher frequencies, however the difference is not significant. The damping values for both bilge keels is probably overestimated, due to the large time-step. Nevertheless, both bilges appear to provide a large amount of damping.

4.3 Wave Response

For wave response a time-step of $\delta t = 0.001$ is chosen, with a mesh base size of 0.5, which results in a very computational demanding simulation. Thus the amount of simulations conducted is severely reduced, which means that fewer frequencies can be tested. Since the area of most interest is near resonance, the frequency of incoming waves is set to be near the eigenfrequency in roll. The eigenfrequency is found from the well known formula for eigenperiod in roll (Faltinsen, 1993):

$$T_{4n} = \sqrt{\frac{I_{44} + a_{44}}{\rho g \nabla GM}} \tag{4.1}$$

The metacentric height ($GM = 0.04667$) is found as described in chapter 2.5.3, and the roll inertia (I_{44}) is set to be $2.1333[\frac{kg}{m^2}]$. The added roll inertia can be found by interpolation of either the experimental data or the simulation results. However, the two coefficients results in different eigenfrequencies. By use of Vugts experimental values the eigenfrequency becomes $\omega \sim= 3.7$ while the coefficient found by simulation results in $\omega \sim= 3.5$. The middle value ($\omega = 3.6$) is chosen as the incoming wave frequency.

The roll angle response from the waves is shown as a time series in figure 4.10.

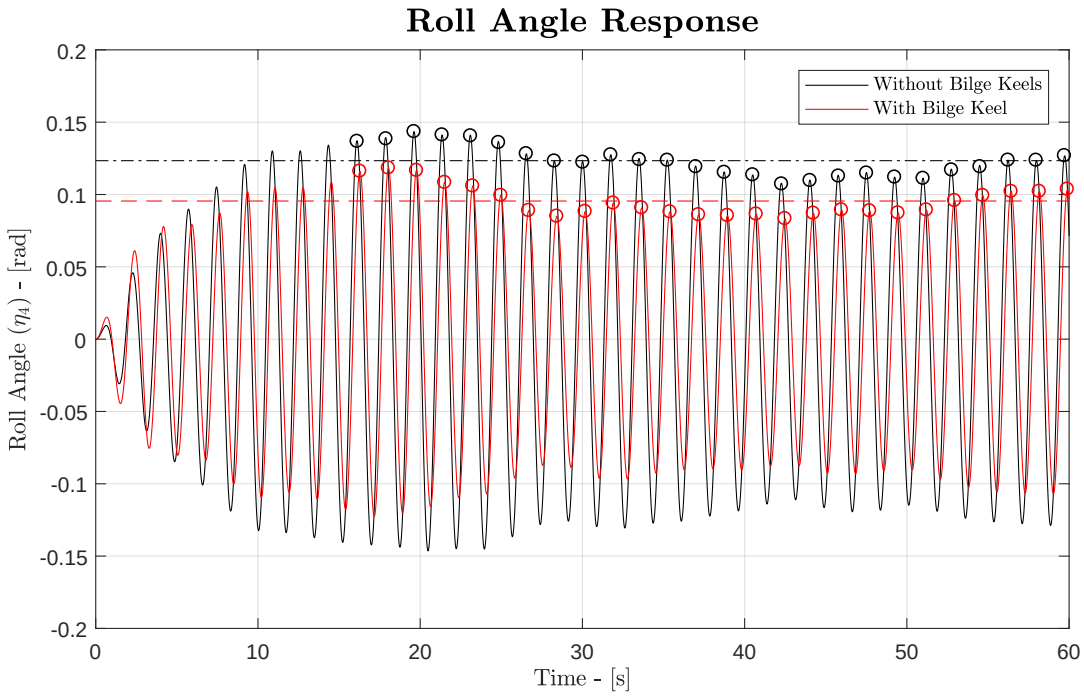

Figure 4.10: Roll angle response time series for incoming waves, for cross sections with and without bilge keels

As previously discussed, the damping is highly non-linear. Therefore, in order for the response to be comparable with the rest of the results, a wave height that produces response am-

plitudes near the harmonic motion amplitude ($\eta_{4,a} \sim= 0.1$) is necessary. Based of some experience and some rough mesh-testing, a wave height of 0.02m is chosen.

To quantify the difference in motion amplitude, the mean of all peaks in the time range $t \in [15,60]$ (seconds) is calculated. The peaks used and the calculated mean is marked with circles and as dashed lines in figure 4.10. The mean bilge keel amplitude is 77.4% of the bare hull amplitude, which is a significant reduction in response.

Since the eigenfrequency is dependent upon added inertia, which is different for the two hulls, the resonance period might not be equal for both hulls. It has been shown that the introduction of bilge keels increase the added inertia (Yeung et al., 2001), which is consistent with the simulation results found in this thesis.

In addition, the true resonance occurs at the damped eigenfrequency, which is given by the relationship $\omega_d = \omega_n\sqrt{1-\xi^2}$, where ξ is the damping ratio. While the damped eigenfrequency is often assumed equal to the undamped eigenfrequency in roll due to the low amount of damping, the introduction of bilge keels makes this assumption less valid.

Therefore, it is reasonable to assume that the increased added inertia and damping due to the bilge keels will decrease resonance frequency slightly. The comparison in mean roll amplitude above therefore might be misleadingly low. In order to inspect this the response must be found for an entire range of frequencies, but due to time constraints this is not done.

A further complication is the non-linearity of both added inertia and damping. It has been shown both experimentally and numerically (Vugts (1968),Yeung et al. (2001)) that added roll inertia is amplitude dependent.

In table 4.2 the roll amplitudes for both cross sections is listed.

Table 4.2: The mean peak values, in the time range 15-60 seconds

	No Bilge Keel	Bilge Keel
$\eta_{4,a}$	0.12338	0.09549
$\frac{\eta_{4,a}}{k\zeta_a}$	9.33925	7.22828

4.4 Flow separation

In figure 4.11 the flow past the upstream corner from the wave response simulations is shown for the cross section with bilge keel.

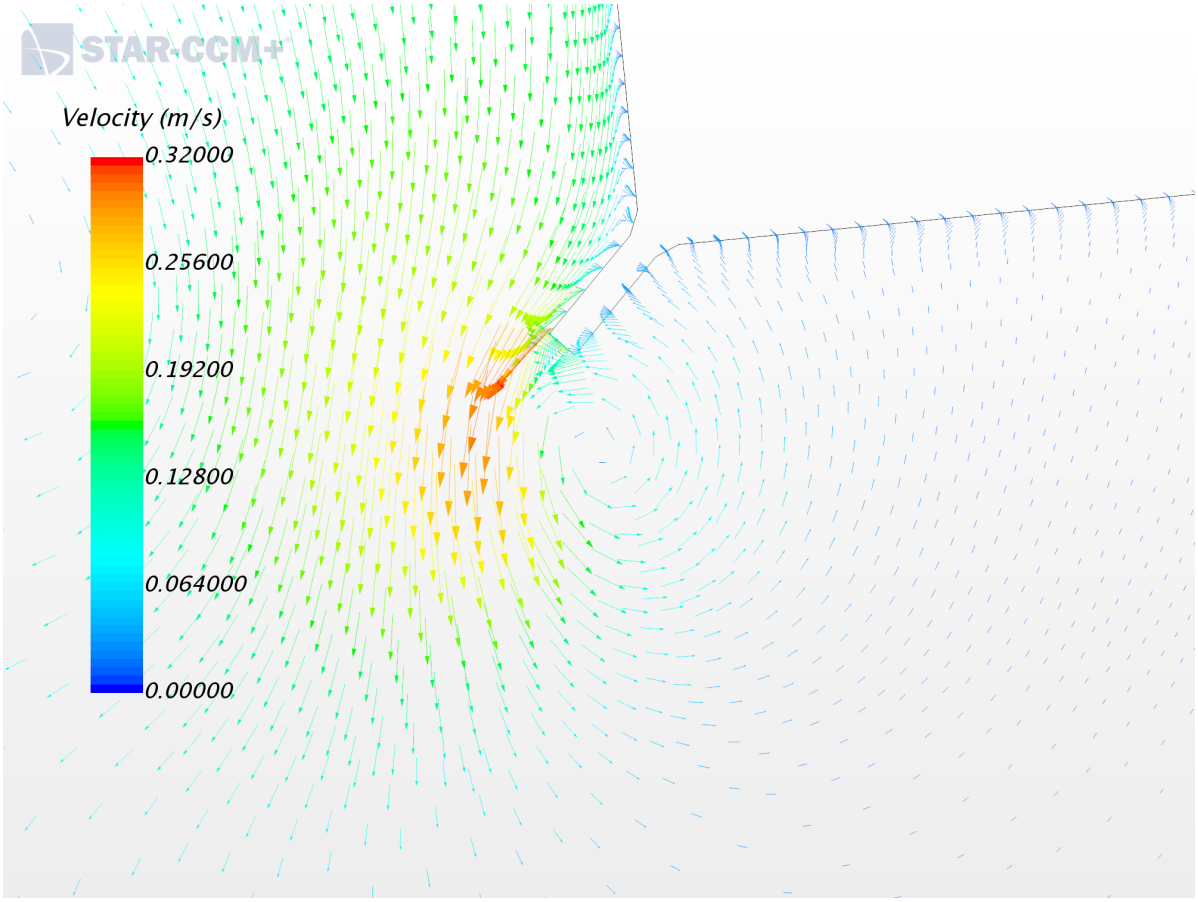

Figure 4.11: Velocity glyph of the flow past the upstream corner, at t=60s and a roll angle of $\eta_4 = \sim 0.1$

As the figure 4.11 illustrates, the flow near the bilge keel is complex. The flow past the bilge keel tip has an increased velocity, with a large vortex in the bilge keels wake. Above the bilge keel, in figure4.11, back flow is occurring upwards along the hull. Backflow is due to the no-slip condition of the wall boundary, which means that the fluid next to the wall must follow the wall velocity from the rotational motion. Flow separation and vortex shedding occurs for both hull with and without bilge keels for simulations of wave response and harmonic motion. This is illustrated in figure 4.12

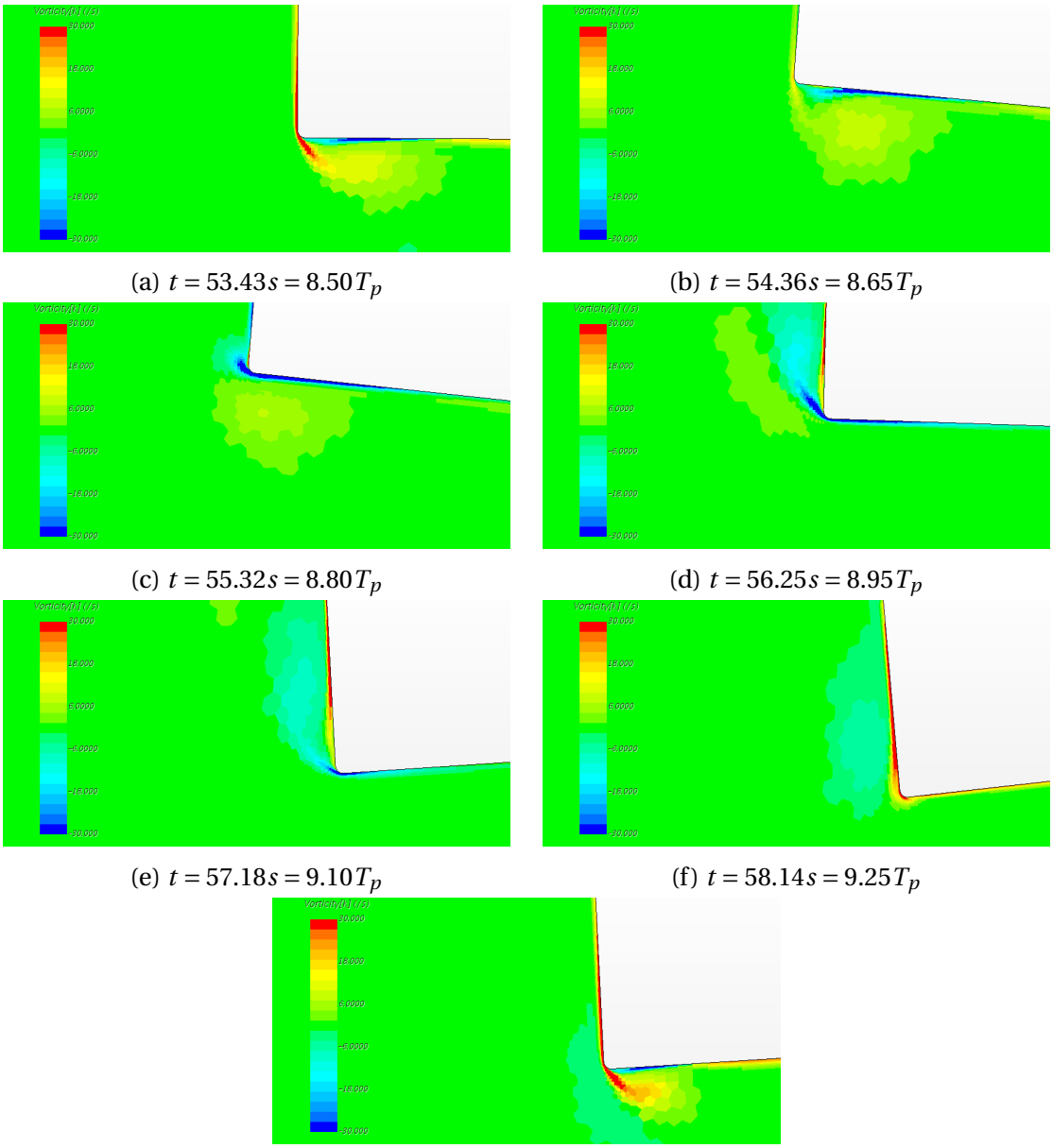

(a) $t = 53.43s = 8.50T_p$

(b) $t = 54.36s = 8.65T_p$

(c) $t = 55.32s = 8.80T_p$

(d) $t = 56.25s = 8.95T_p$

(e) $t = 57.18s = 9.10T_p$

(f) $t = 58.14s = 9.25T_p$

(g) $t = 59.07s = 9.40T_p$

Figure 4.12: Vorticity plots for one period ($T_p = \frac{2\pi}{\omega}$), for a frequency of $\omega = 1$.

Figure 4.12 shows the shedding of vortexes over one period of harmonic imposed motion. The geometry is equal to the experimental design of Vugts (1968), as described in chapter 2.3. The vorticity behavior is shown for a developed flow in the time interval $8.5T_p < t < 9.4T_p$.

Illustrated in 4.12a, flow past the cross section corner causes a vortex of recirculating fluid in its wake. As the roll motion turns, the vortex is shed (4.12b and 4.12c) and a counter rotating vortex starts to develop. Following, the separated vortex shifts past the corner and moves up along the hull (4.12d and 4.12e) while the counter rotating vortex becomes fully developed. When the roll motion reaches a minimum, an inverse repetition of the peak roll motion flow

occurs. Quérard et al. (2009) reported that simulations with larger time-steps results in lower vorticity values for separated vortexes.

Chapter 5

Summary, Conclusion and Further Work

In this thesis 2D dimensional CFD simulations on rectangular cross sections of varying corner radius, both fitted with and without bilge keels, has been conducted. Imposed harmonic motion and wave response has been simulated, and the two dimensional coefficients has been calculated using both a linearized damping model and Yeung's composite model for a range of frequencies. The coefficients are compared to previously established experimental results. The free floating wave-response has been presented for waves near the eigenfrequency for a single cross section both with and without bilge keels.

The simulations has shown to capture roll damping accurately given sufficiently low time steps and mesh density. The simulation approach has proved to have difficulties in accurately capture the added roll inertia, which is consistent with other RANS simulations. Increase in damping when fitting the geometry with bilge keels has been shown for cross sections of small and large corner radius, in both wave response and harmonic motion. However, the magnitude of damping due to bilge keels is not accurately captured due to large computational power and time required.

Bilge keel length has shown to have a significant impact on the damping provided, with longer bilge keels producing more damping. The linearized damping coefficient for cross sections fitted with bilge keels has similar form to other experimental results done with bilge keel fitted rectangular cylinders. Using Yeung's composite model, the bilge keel has shown to have little to no impact on the wave-damping while a very significant impact on the quadratic damping. An reduction of roll motion response amplitude by fitting a cross section with bilge keels has been documented.

5.1 Further Work

Further work can include a harmonic motion experimental test for a bilge keel fitted cross section in order to find the accurate roll damping for a range of frequencies, possible conducted in parallel with CFD simulations that utilizes a lower time-steps. It is of interest to both experimentally test and simulate wave-response for rolling cross sections with and without bilge keels for a range of wave-frequencies, in order to find a complete response amplitude operator.

A literature study that tries to quantify which RANS turbulence models that might more accurately capture the added roll inertia is recommended.

Bibliography

Faltinsen, O. (1993). *Sea loads on ships and offshore structures*, volume 1. Cambridge university press.

Froude, W. (1865). On the practical limits of the rolling of ships in a sea-way.

Ikeda, Y., Himeno, Y., and Tanaka, N. (1977a). On eddy making component of roll damping force on naked hull. *Journal of the society of Naval Architects of Japan*, 1977(142):54–64.

Ikeda, Y., Komatsu, K., Himeno, Y., and Tanaka, N. (1977b). On roll damping force of ship-effect of hull surface pressure created by bilge keels. *Journal of Kansai Society of Naval Architects*, 165:31–40.

J. Amdahl, A. Endal, e. A. (2015). Marin teknikk grunnlag : Tmr4105 : kompendium.

Jones, W. and Launder, B. (1972). The prediction of laminarization with a two-equation model of turbulence. *International journal of heat and mass transfer*, 15(2):301–314.

Kato, H. (1965). Effects of bilge keels on the rolling of ships. *Journal of Zosen Kiokai*, 1965(117):93–101.

Menter, F. R. (1994). Two-equation eddy-viscosity turbulence models for engineering applications. *AIAA journal*, 32(8):1598–1605.

Pettersen, B. (2007). *Kompendium TMR4247; Marin Teknikk 3 - Hydrodynamikk*.

Quérard, A., Temarel, P., and Turnock, S. (2009). The hydrodynamics of ship-like sections in heave, sway, and roll motions predicted using an unsteady reynolds-averaged navier—stokes method. *Proceedings of the Institution of Mechanical Engineers, Part M: Journal of Engineering for the Maritime Environment*, 223(2):227–238.

Rodi, W. (1991). Experience with two-layer models combining the k-epsilon model with a one-equation model near the wall. In *29th Aerospace sciences meeting*, page 216.

SIEMENS (2017). *STAR-CCM+ Documentation, Version 12.02*.

Vugts, J. (1968). The hydrodynamic coefficients for swaying, heaving and rolling cylinders in a free surface. Report.

Yeung, R., Liao, S.-W., and Roddier, D. (1998). Hydrodynamic coefficients of rolling rectangular cylinders. *International Journal of Offshore and Polar Engineering*, 8(04).

Yeung, R., Roddier, D., Alessandrini, B., Gentaz, L., and Liao, S. (2001). On roll hydrodynamics of cylinders fitted with bilge keels.

Yeung, R. and Vaidhyanathan, M. (1994). Highly separated flows near a free surface. pages 118–128.

Appendix A

Complete List of Physics Models

Following is a complete list of all physics models used for this thesis, in alphabetical order. For brief explanations see subsection 2.2, for an in detail description the STAR-CCM+ user manual is refereed to (SIEMENS, 2017).

- Eulerian Multiphase
- Exact Wall Distance
- Gradients
- Gravity
- Implicit Unsteady
- K-Epsilon Turbulence
- Multiphase Equation of State
- Multiphase Interaction
- Reynolds-Averaged Navier-Stokes
- Segregated Flow
- Turbulent
- Two Dimensional
- Two-Layer All y+ Wall Treatment
- Volume of Fluid (VOF)

Appendix B

Vugts Experimental Results

Following is a scan of the added inertia and damping coefficients found experimentally by Vugts (1968). Note that the nomenclature is different from the thesis, with $a_{\phi\phi}$ being roll inertia, $b_{\phi\phi}$ being roll damping, and the coupled sway-roll terms represented as $a_{y\phi}$ and$b_{y\phi}$. A is the submerged area. All other nomenclature is consistent with the thesis.

The coupled coefficients has a different sign convention, and is therefore shown as negative values. When used in the thesis the experimental results from the coupled coefficients are converted to a positive sign convention.

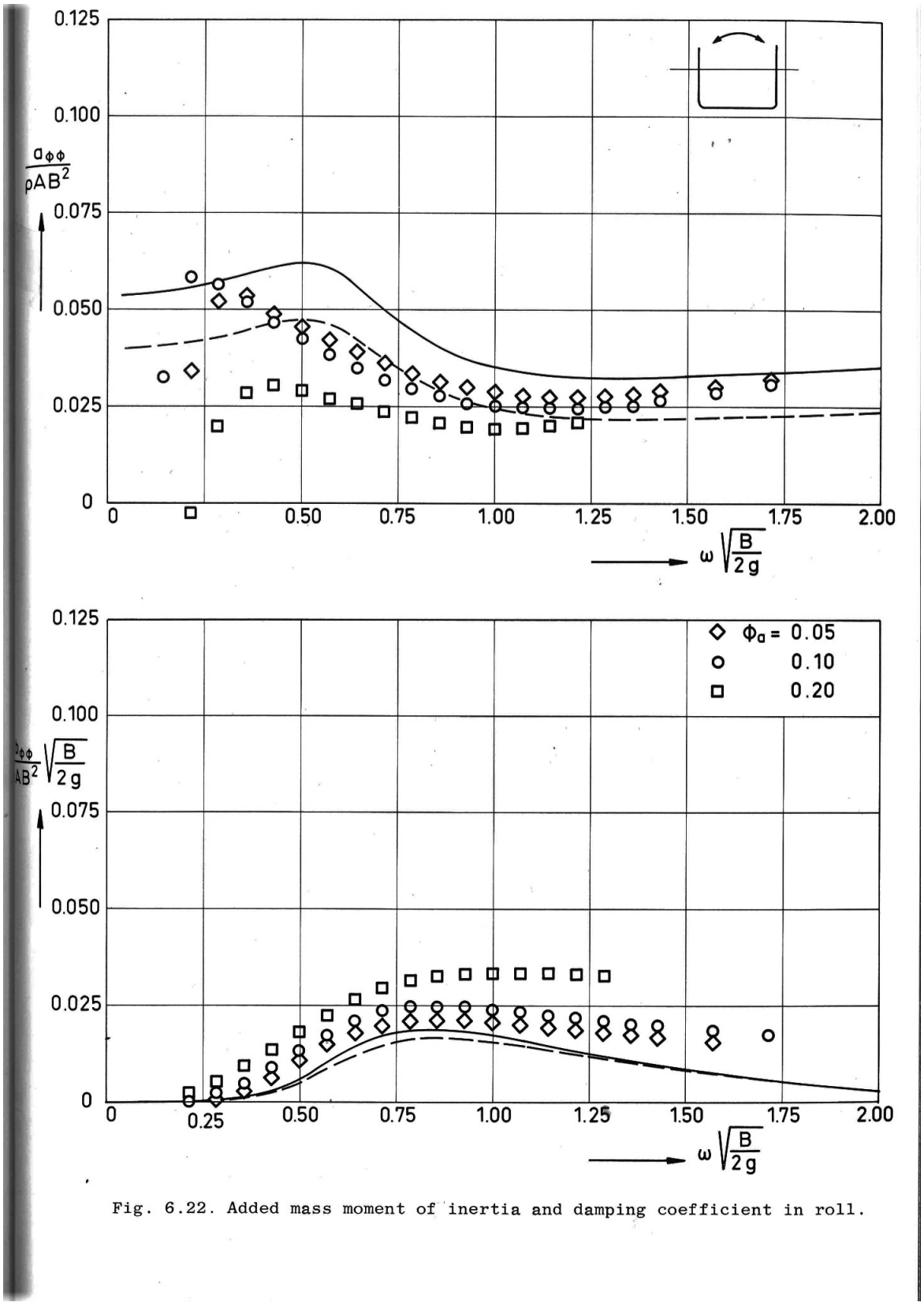

Fig. 6.22. Added mass moment of inertia and damping coefficient in roll.

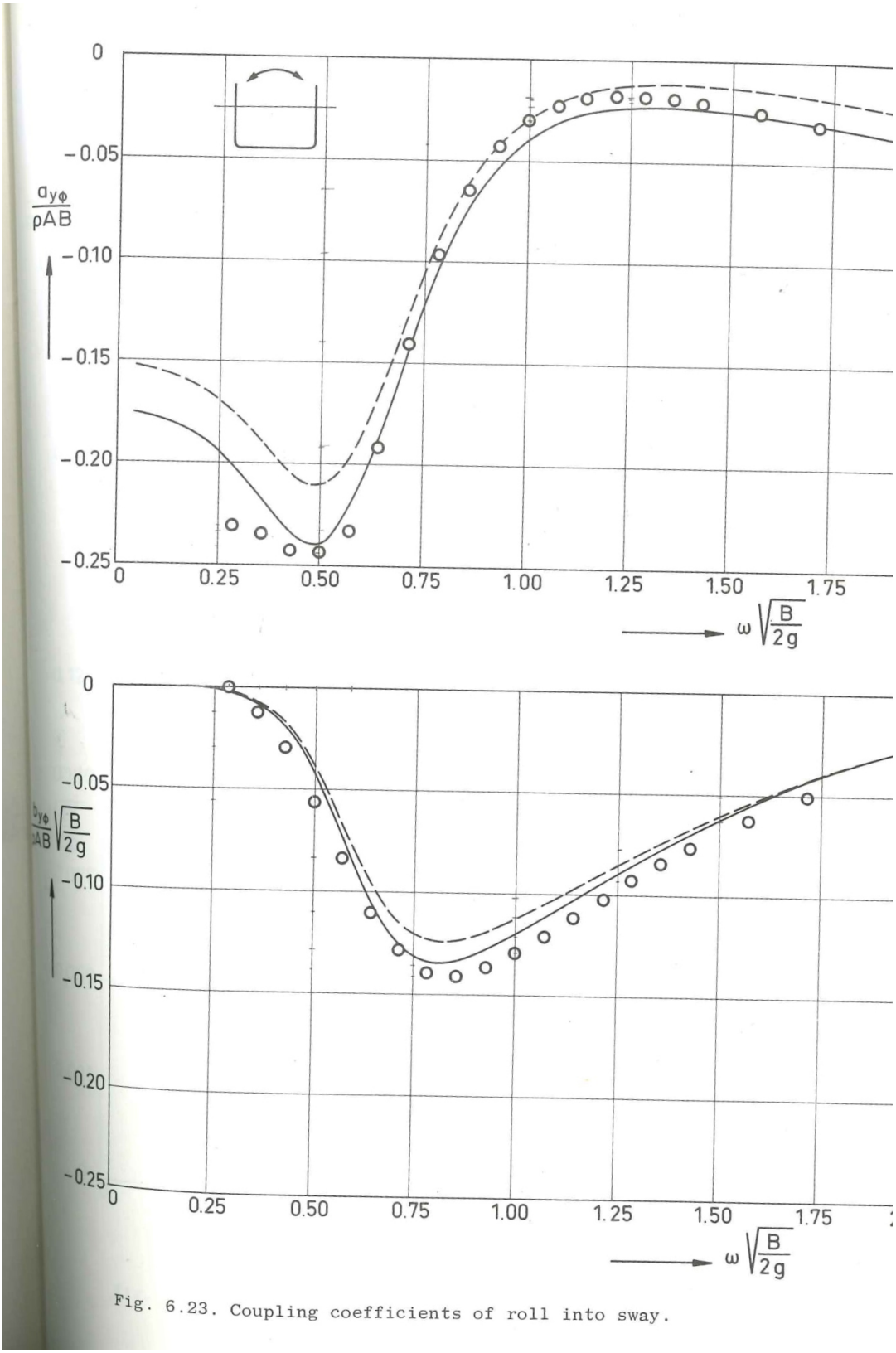

Fig. 6.23. Coupling coefficients of roll into sway.

Appendix C

Yeung: Experimental And Simulation Results

Following is a page from "Hydrodynamic Coefficients of Rolling Rectangular Cylinders" by Yeung et al. (1998) that shows coupled and uncoupled added inertia and linearized damping coefficients. The coefficients are found both by use of a free-surface random vortex method simulation and experiments. Note that, the harmonic motion amplitude applied in this thesis is approximately equal to a roll angle of 5.75 degrees.

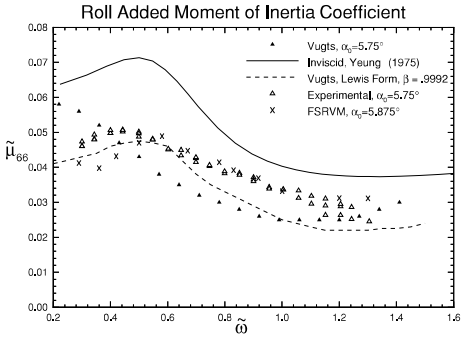

Fig. 9 Added moment of inertia coefficient, $\alpha_0 = 5.75°$

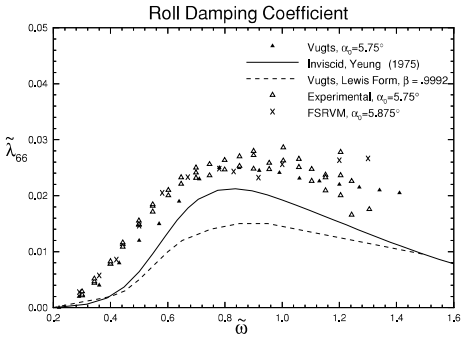

Fig. 10 Damping coefficient, $\alpha_0 = 5.75°$

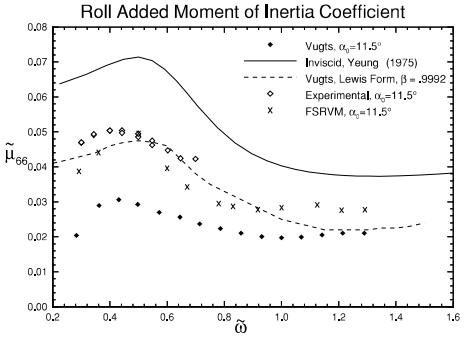

Fig. 11 Added moment of inertia coefficient, $\alpha_0 = 11.5°$

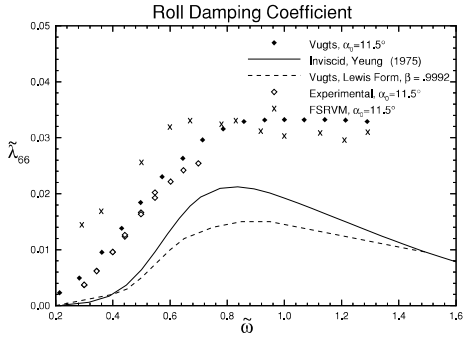

Fig. 12 Damping coefficient, $\alpha_0 = 11.5°$

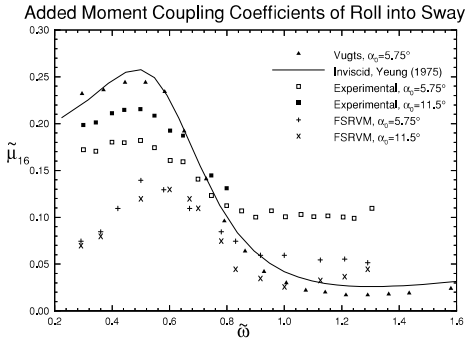

Fig. 13 Added moment coupling coefficient

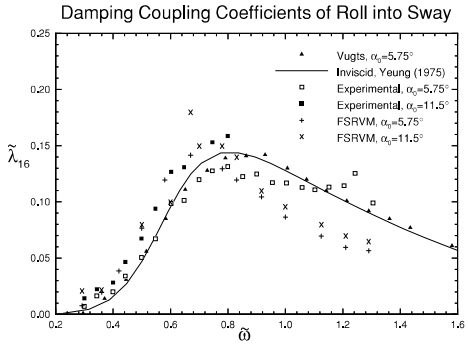

Fig. 14 Damping coupling coefficient

$$M_w(t) = -\mu_{66}\ddot{\alpha} - \lambda^*_{66}\dot{\alpha} - \lambda^e_{66}\dot{\alpha}|\alpha|. \quad (41)$$

The asterisk, *, is used to distinguish these coefficients from those in Eqs. 31 and 39.

To determine these two coefficients uniquely, we argue that the *time-averaged* mechanical power, W, that needs to be input to sustain the rolling motion can be decomposed into two parts, $\dot{W} = \dot{W}_w + \dot{W}_d$, where $\dot{W}_w$ represents dissipation due to radiation effects and $\dot{W}_d$ represents that caused by viscous effects. $\dot{W}_w$ would show up in the far fields as the energy fluxes of the radiated waves, say of amplitudes A_+ and A_- (see Fig. 4). It is easy to show, using the concept of group velocity, that the *time-averaged* energy flux is given by:

Appendix D

MATLAB Functions

MATLAB is utilized for several post-processing calculations, creation of plots and data management. A complete script of all calculations and plot/files generated would be too long to include in the appendix. However, the functions that calculate the most essential values and coefficients are included. Following is a list of the functions used and their theory description, after which comes the function codes.

- **GZ2:** The calculation of restoring moment arm for 2.5 mm cross sections. Described in chapter 2.7.1
- **GZ3:** The calculation of restoring moment arm for 50 mm cross sections. Described in chapter 2.7.1
- **Coeff:** Calculates the hydrodynamic coefficients from a moment/force time series. Described in chapter 2.7.2
- **Coeff w:** Calculates the Yeung's composite model wave-damping coefficient from an wave-amplitude time series. Described in chapter 2.7.3
- **Coeff q:** Calculates the Yeung's composite model quadratic-damping coefficient from an wave-amplitude time series. Described in chapter 2.7.3

```
function [Cx, A] = GZ2(e,T);

R = [cos(e) sin(e);-sin(e) cos(e)];
V1 = [T,-T];
V2 = [-T,-T];
rV1 = (R*V1')';
rV2 = (R*V2')';
C1 = [T/cos(e),0];
C2 = [-T/cos(e),0];
P = [C1;rV1;rV2;C2;];
Ai = zeros(length(P)-1,1);
for i = 1:length(P)-1
    Ai(i) = P(i,1)*P(i+1,2) - P(i+1,1)*P(i,2);
    Cxi(i) = (P(i,1)+P(i+1,1))*(P(i,1)*P(i+1,2) - P(i+1,1)*P(i,2));
end
A = 0.5*sum(Ai);
Cx = (1/(6*A))*sum(Cxi);
```

Published with MATLAB® R2017a

```
function [Cx, A] = GZ3(e,T,B,Ra);
try
    temp = Ra;
catch
    Ra = 0.05;
    B = 0.4;
end
R = [cos(e) sin(e);-sin(e) cos(e)];
V1 = [(-0.5*B),(-T+Ra)];
V2 = [(-0.5*B)+Ra*(1-cos(pi/6)),-T+Ra*(1-sin(pi/6))];
V3 = [(-0.5*B)+Ra*(1-sqrt(2)/2),-T+Ra*(1-sqrt(2)/2)];
V4 = [(-0.5*B)+Ra*(1-cos(pi/3)),-T+Ra*(1-sin(pi/3))];
V5 = [-0.5*B+Ra,-T];
V6 = [0.5*B-Ra,-T];
V7 = [(0.5*B)-Ra*(1-cos(pi/3)),-T+Ra*(1-sin(pi/3))];
V8 = [(0.5*B)-Ra*(1-sqrt(2)/2),-T+Ra*(1-sqrt(2)/2)];
V9 = [(0.5*B)-Ra*(1-cos(pi/6)),-T+Ra*(1-sin(pi/6))];
V10 = [0.5*B,-T+Ra];
V = [V1;V2;V3;V4;V5;V6;V7;V8;V9;V10];
rV1 = (R*V1')';
rV2 = (R*V2')';
rV3 = (R*V3')';
rV4 = (R*V4')';
rV5 = (R*V5')';
rV6 = (R*V6')';
C1 = -0.5*B*[sin(e)*tan(e) + cos(e),0];
C2 = 0.5*B*[sin(e)*tan(e) + cos(e),0];
C =[C1;C2];
P(1,:) = C1;
for i = 1:length(V)
   P(i+1,:) = (R*V(i,:)')';
end
P(end+1,:) = C2;
Ai = zeros(length(P)-1,1);
for i = 1:length(P)-1
    Ai(i) = P(i,1)*P(i+1,2) - P(i+1,1)*P(i,2);
    Cxi(i) = (P(i,1)+P(i+1,1))*(P(i,1)*P(i+1,2) - P(i+1,1)*P(i,2));
end
A = 0.5*sum(Ai);
Cx = (1/(6*A))*sum(Cxi);
```

Published with MATLAB® R2017a

```
function [a44, b44, T, a44_, b44_, Tvar, timeS] = coeff(Time, Moment,
 amp, tRange, visc, T)

% % If viscosity isn't stated, fresh water is assumed:
try
    temp = visc;
catch
    visc = 8.88715*10^-4;
end
clear('temp');

% % If the period isn't stated, an estimate
% % is calculated (not absolutely not recommended):
try
    temp = T;
catch
    [pks t_pks] = findpeaks(Moment,Time);
    for i = length(t_pks):-1:2
        if pks(i) < 0
            t_pks(i) = [];
            pks(i) = [];
        elseif abs(t_pks(i-1)-t_pks(i)) < 0.3
            if t_pks(i) < t_pks(i-1)
                t_pks(i) = [];
                pks(i) = [];
            else
                t_pks(i-1) = [];
                pks(i-1) = [];
            end
        elseif pks(i) < pks(i-1)
            if pks(i)/pks(i-1) < 0.9
                pks(i) = [];
                t_pks(i) = [];
            end
        end
    end
    if pks(1) < 0
        pks(1) = [];
        t_pks(1) = [];
    end

    T = mean(diff(t_pks));
end
clear('temp');

% % If the integration range isn't stated
% % an estimate is calculated (not absolutely not recommended):
try
    temp = tRange;
catch
    tRange = [min(Time),max(Time)];
end
```

```
function [b44_w b44_w_ maxA1 maxA2,tlim] = coeff_w(A1, A2, Time, w,
 amp, mA1, mA2, tRange)
mStatus = 1;
try
    temp = tRange;
catch
    tRange = [Time(0) Time(end)];
end
try
    temp = mA1;
    temp = mA2;
catch
    mStatus = 0;
end
T = 2*pi/w;
g = 9.81;
rho = 997;

for i = 1:length(Time)
    if Time(i) < tRange(1)
    elseif Time(i) > tRange(1)
        iRange(1) = i;
        break
    end
end

tRange(1) = Time(iRange(1));
t = (tRange(1)+T/2):mean(diff(Time)):(tRange(2)-T/2);
tlim = [t(1) t(end)];

if mStatus == 0
    A1 = (A1-mean(A1))/2;
    A2 = (A2-mean(A2))/2;

    maxA1 = max(A1);
    maxA2 = max(A2);
    for i = 1:length(t)
        t0 = t(i);
        iMin = 1;
        iMax = length(Time);
        tMin = min(Time);
        tMax = max(Time);
        for u = 1:length(Time)
            if abs(Time(u) - (t0 - T/2)) < abs(tMin-(t0 - T/2))
                tMin = Time(u);
                iMin = u;
            end
            if abs(Time(u) - (t0 + T/2)) < abs(tMax-(t0 + T/2))
                tMax = Time(u);
                iMax = u;
            end
        end
```

```
function [b44q b44q_] = coeff_q(Time,Moment,w,amp,T,tRange);
t = (tRange(1)+T/2):mean(diff(Time)):(tRange(2)-T/2);
for i = 1:length(t)
    t0 = t(i);
    iMin = 1;
    iMax = length(Time);
    tMin = min(Time);
    tMax = max(Time);
    for u = 1:length(Time)
        if abs(Time(u) - (t0 - T/2)) < abs(tMin-(t0 - T/2))
            tMin = Time(u);
            iMin = u;
        end
        if abs(Time(u) - (t0 + T/2)) < abs(tMax-(t0 + T/2))
            tMax = Time(u);
            iMax = u;
        end
    end
    timeInterv = Time(iMin:1:iMax);
%     [iMin tMin iMax tMax]
    func = Moment(iMin:1:iMax).*cos(w*Time(iMin:1:iMax));
    b44q_(i) = -(3/(8*amp*amp*w))*trapz(timeInterv,func);
end
b44q = mean(b44q_);
```

Published with MATLAB® R2017a